Benchmarking of Photocatalytic Pigments for Coating Applications

Ana Carolina Ferreira da Silva Vaz

Thesis to obtain the Master of Science Degree in

Chemical Engineering

Advisor(s)/Supervisor(s): Dr. Auguste Fernandes
Dr. Amado Andrés Velázquez-Palenzuela

Examination Committee

Chairperson: Dr. José Nuno Aguiar Canongia Lopes
Advisor: Dr. Maria Filipa Gomes Ribeiro
Dr. Amado Andrés Velázquez-Palenzuela

November 2021

Acknowledgments

Abstract

Photocatalytic coatings are a broad field of study where these films are proved to provide the applied surfaces several features such as self-cleaning properties, anti-fouling/anti-bacterial properties, and degradation of pollutants features. The pigments adopted in the formulation of these coatings are responsible for this behavior. This component, when under the action of light, may prompt reactions which favour the aforementioned applications. TiO_2 nanoparticles (NPs) are one of the most used as photocatalytic pigments. However, EU published a statement in 2020 acknowledging its toxicity by inhalation and its potential carcinogenic risks. Regulations applied on this suspected carcinogen material, triggered the need to find healthier and more environmentally-friendly alternatives. To evaluate feasible alternative as substitutes for TiO_2, and also to compare alternatives among them, a benchmarking approach was taken. This way, TiO_2-based photocatalysts, as well as non-TiO_2-based photocatalysts, most of them already in use in coatings industry as functional pigments were confronted. TiO_2 Rutile, TiO_2 Anatase, TiO_2 P25, ZnO, Fe_2O_3 spherical, Fe_2O_3 lamellar, FeOOH, and Cu_2O were successfully characterized and tested. The characterization techniques involved X-Ray Diffraction (XRD) and Differential Reflectance Spectroscopy (DRS). The first, revealed the structure, the relative quantity of each present phase, and the cristallite size. DRS along with the Kubelka-Munk equation gave out the band gap value. In order to evaluate on the photocatalyst perfomance was evaluated under two kinds of light sources were used: UV-C and UV/Visible light. A slurry containing the chosen dye (methylene blue) and the photocatalyst was prepared and the ability of the latter to degrade the first was evaluated under the two types of light source measuring the absorbance in a spectrophotometer. Of all the non-TiO_2-based alternatives studied, ZnO showed the best performance under both types of light when compared with TiO_2-based samples. Due to that fact, ZnO was elected the alternative to TiO_2-based photocatalysts. All the Fe-based and Cu_2O showed no MB degradation in both scenarios. The wide band gap, as well as the valance and conduction band (VB/CB) positions may explain the better performance of ZnO towards the TiO_2-based photocatalysts. The wider band gap that allows the absorption of high energy sources of light (as in UV), and the position of the VB/CB enables the reduction and oxidation reactions to occur, which both make the sample active. The formulation of coatings with ZnO should be carried out and its performance studied under the same conditions. All the Fe-based and Cu_2O that showed no MB degradation in both scenarios, should be submitted to other conditions (irradiation with visible light) to evaluate their performance under this type of light.

Keywords: Coatings; photocatalysis; semiconductor; methylene blue photodegradation; non-TiO2 based photocatalysts; TiO2 nanoparticles; toxicity; X-ray diffraction; UV/Vis Diffuse reflectance spectroscopy; UV light source.

Resumo

Os revestimentos fotocatalíticos são um vasto campo de estudo onde se provou fornecem às superfícies aplicadas várias características tais como propriedades de auto-limpeza, características anti-incrustantes/anti-bacterianas, e degradação de poluentes. Os pigmentos adoptados na formulação destes revestimentos são responsáveis por este comportamento. Este componente, quando sob a acção da luz, pode provocar reacções que favorecem as aplicações acima mencionadas. As nano-partículas de TiO_2 são das mais utilizadas como pigmentos fotocatalíticos. No entanto, a UE publicou uma declaração em 2020 reconhecendo a sua toxicidade por inalação e os seus potenciais riscos car-cinogénicos. Os regulamentos aplicados a este material suspeito de ser cancerígeno, desencadearam a necessidade de encontrar outras alternativas. Para avaliar a viabilidade da alternativa como um subs-tituto do TiO_2, e também para comparar as alternativas entre elas, foi adoptada uma abordagem de *benchmarking*. Desta forma, os fotocatalisadores baseados em TiO_2, bem como os fotocatalisadores não baseados em TiO_2, a maioria deles já em uso na indústria de revestimentos como pigmentos funci-onais, foram confrontados. Como fotocatalisadores baseados em TiO_2, TiO_2 Rutilo, TiO_2 Anatase, TiO_2 P25 foram seleccionadas, bem como algumas potenciais alternativas não baseadas em TiO_2, nome-adamente Fe_2O_3 esféricas, Fe_2O_3 lamelares, $FeOOOH$ e Cu_2O todas caracterizadas e testadas com sucesso. As técnicas de caracterização envolveram Difracção de Raio-X (DRX) e Espectroscopia de Reflectância Diferencial (DRS). A primeira, revelou a estrutura, a quantidade relativa de cada fase pre-sente, e o tamanho do cristalito. Já a última técnica, e recorrendo à equação de Kubelka-Munk, foi possível obter o valor do Band Gap. O desempenho de cada fotocatalisador foi avaliado sob dois tipos diferentes de fontes de luz: UV-C e UV/Luz Visível. Foi preparada uma mistura de corante azul de me-tileno e fotocatalisador. A fotodegradação do corante azul de metileno por parte do fotocatalisador foi avaliada sob os dois tipos de fontes de luz medindo a absorvância da mistura num espectrofotómetro. De todas as alternativas não baseadas em TiO_2 estudadas, foi o ZnO que mostrou o melhor desem-penho sob ambos os tipos de luz, sendo a alternativa eleita aos fotocatalisadores baseados em TiO_2. Todos as amostras de Fe e Cu_2O não mostraram degradação do MB em ambos os cenários. A largura da banda, bem como as posições da banda de valência e da banda de condução (BV/BC) podem expli-car o melhor desempenho do ZnO em relação aos fotocatalisadores baseados em TiO_2. A maior largura da banda que permite a absorção de fontes de luz de alta energia (como UV), e a posição da BV/BC permite a ocorrência de reacções de redução e oxidação, o que tornam a amostra activa. A formulação de revestimentos com ZnO deve ser realizada e o seu desempenho estudado nas mesmas condições. Todas as amostras com Fe e Cu_2O que não mostraram degradação MB em ambos os cenários, devem ser submetidas a outras condições (irradiação com luz visível) para avaliar o seu desempenho sob este tipo de luz.

Keywords: Revestimentos; fotocatálise; semicondutor; fotodegradação de azul de metileno; fotocatalisadores não baseados em TiO2; nanopartículas de TiO2; toxicidade; difracção de raio-X; espectroscopia de reflectância difusa UV/Vis; fonte de luz UV.

Contents

x

List of Tables

List of Figures

Nomenclature

Abbreviations

BET Brunauer-Emmett-Teller theory

CB Conduction Band

$CoaST$ Coatings Science and Technology Centre

COD Crystallography Open Database

DLS Dynamic Light Scattering

DNA Deoxyribonucleic acid

DRS UV-Vis Diffuse Reflectance Spectroscopy

DW Distilled water

$ECETOC$ European Centre for Ecotoxicology and Toxicology of Chemicals

EPA Environmental Protection Agency

EU Europeand Union

$FWHM$ Full width at half maximum

IR Infrared

$ISEL$ Instituto Superior de Engenharia de Lisboa

IST Instituto Superior Técnico

LMB Leucomethylene Blue

NP Nanoparticle

PC Photocatalytic

PDF Powder Diffraction File

SEM Scanning Electron Microscopy

SPM Scanning Probe Microscopy

TEM Transmission Electron Microscopy

TGA Thermogravimetric Analysis

US United States

UV	Ultraviolet
VB	Valance Band
Vis	Visible
XRD	X-Ray Powder Diffraction

Symbols

α	Absorption
β	Full width at half maximum
λ	Wavelength
σ	Area occupied by an adsorbate molecule
θ	Bragg's diffraction angle
C	Concentration of the dye
c	Adsorption enthalpy of the first layer
C_0	Concentration of the dye in the beginning
ct	Enthalpy of adsorption for the first layer
Eg	Optical band gap energy
$e_{cb}{}^-$	Electron
$F(R_{inf})$	Diffuse reflectance
h	Hour
h	Planck's constant
hv	Photon energy
$h_{vb}{}^+$	Hole
k_a	Equilibrium constant of the reactant
k_r	Specific reaction rate constant for the oxidation of the reactant
mg	Milligram
min	Minutes
mL	Milliliter
mm	Millimeter
n	Type of electronic transition
nm	Nanometer
P	Pressure
P/P_0	Relative pressure

P/P_0	Relative pressure
ppm	Part per million
r	Reaction rate
R_{inf}	Remission fraction of an infinitely thick layer
t	Time
v	Speed of light
V_A	Adsorbed volume
V_M	Monolayer volume
V_M	Volume of the monolayer
x_{dry}	Weight fraction in the solid on a dry basis
	Degree angle
C	Degree Celsius
$\mathring{A}$	Angstrom

Chapter 1

Introduction

A coating, commonly known as paint or varnish, is a layer of material that is applied to a surface that may acquire several purposes, such as decorative or protective purposes [10]. Photocatalysis is a process that nature created, also known as photosynthesis, and humans mimicked. In this mechanism, photocatalytic (PC) materials when hit by light, may prompt chemical reactions. The association between a coating material and a PC element gave rise to a versatile technology with multiple applications. Having light as the driving force, the final applications are the most diverse - from self-cleaning surfaces to the degradation of air pollutants, and the inactivation of viruses and bacteria [11, 12].

Even though PC coatings contribute to the sustainable development of communities, which is following UN's Sustainable Development Goals [13], some drawbacks that need to be addressed - poor activity under visible light or unstable coatings are some well-known problems. Recently, the widely used TiO_2 NPs have been defined as a suspicious carcinogen to humans by inhalation by the EU Regulation on classification, labelling and packaging (CLP) of substances and mixtures [14]. As these harmful effects are being brought to light, political entities are putting pressure on the scientific community to come up with new ideas to solve these problems.

The ultimate goal of this project is to find feasible alternatives to the TiO_2 NPs already in use. Priority was given to those available functional pigments once they are already in use in the coating industry for non-PC functionalities, including anti-fouling, anti-corrosive, and as colour pigments [10]. For that purpose, a benchmarking process will put non-TiO_2 based pigments against TiO_2-based ones, set as reference. As a result of the literature review on what has been done so far concerning the quest to find alternatives to the TiO_2 NPs, the following materials were studied: Fe_2O_3 (spherical and lamellar), $FeOOH$, ZnO, and Cu_2O. Their PC activity has not been extensively described in the literature, but some works have pointed these semiconductors out as potentially active under UV-Vis light. Their PC activity will be described in this project. Characterization techniques were executed such as X-ray diffraction (XRD) and Diffuse reflectance spectroscopy (DRS). After that, photocatalytic tests were carried out using two types of light sources - UV-C and UV-Vis light (with a spectral distribution closer to sunlight). A slurry composed of one of the pigments and a dye, methylene blue (MB), was prepared and the degradation of the MB was closely monitored by measuring the absorbance of each sample through a spectrophotometer. The performance of each semiconductor was subsequently evaluated by finding the best fitting to its degradation behaviour, which happens to be pseudo-first-order kinetics the order which described best the reaction rate.

Chapter 2

Literature Review

2.1 Coatings

Coatings science is a broad field of study whose first appearance brings back to Greek and Roman's times when those were made out of natural resins. Since those ancient times that coatings technology has made some major breakthroughs, yet has some room for improvement and for new applications. They may have informative or aiding purposes with special physical effects - camouflaging of military equipment, road markings, and optical effects induced by coloured, or metallic pigments. Coatings may also have a functional purpose, being able to modify the application characteristics, appearance, or film properties of coatings [15].

Coating materials may assume liquid, paste or powder form and can create a film after surface application. They are typically composed of binders, solvents, pigments, extenders, additives, and plasticizers. Despite only pigments will be covered in depth in this thesis, the other components will be shortly introduced [15] [10].

- **Binders** are present in every coating material regardless of the application. They are responsible for the formation of a continuous film that adheres to the surface being coated by linking together all the other substances present in the coating material.

- **Solvents** are low viscous substances with the ability to dissolve film-forming agents. They play a major role in the applying coatings process as they are liquids that make coatings fluid enough for application. Solvents evaporate during and after application.

- **Extenders** are responsible for the improvement of mechanical and technological coating properties and for raising the solid content of the paint by filling the empty spaces of the structure. Commonly, they are low cost and mainly used because it reduces the cost of a coating.

- **Additives** may be added in minute quantities and aim to enhance the qualitative and economic success of the coating mixture by altering some intrinsic properties.

- **Plasticizer** is an inert organic substance with a low vapour pressure that may assume a liquid or a solid form. It facilitates the dispersion of the pigments during production, suppresses the tendency of the pigments to sediment, provides flowability to the paint when applying, improves flow during film formation and improves the properties of the coated surface by influencing the surface smoothness or roughness. They also increase the coating durability protecting it from bacterial, mildew or even UV radiation. It is responsible for the good adhesion to the substrate coatings as it provides high levels of hardness and good elasticity at the same time.

2.2 Pigments

Pigments are organic or inorganic insoluble fine particles that remain in the coating after film formation. This component has several purposes, such as providing colour, hiding substrates, modifying the application properties of a coating or even modifying the performance properties of films. Worth mentioning that the characteristics of the pigment, like particle size, may dictate a different outcome. It may affect the colour strength, transparency or opacity, exterior durability or solvent resistance. Depending on the final application, some decisions have to be made when choosing the most adequate pigment. Some particularities deserve some attention, such as the colour, the colour strength, the opacity or transparency, the ease of dispersion, the exterior durability, the heat resistance, the chemical resistance, the water solubility, the solvent solubility, the moisture content, the toxic and environmental hazards, the infrared (IR) reflectance, and, of course, the cost. To note that pigments may present photocatalytic properties, as will be discussed in this project.

Pigments may be divided into many categories. Here, they were divided into white, colour, functional, and nano-pigments.

2.2.1 White Pigments

White pigments may be used alone or with other pigments to provide a lighter colour. The ideal white pigment should absorb no visible light as it should have a high scattering coefficient. To control the scattering coefficient, the refractive index between the pigment and the binder must be regulated.

ZnO and TiO_2 are examples of white pigments. These oxides are the most widely used pigments mainly because of their high photochemical activity, low cost, stability in aqueous systems and chemical stability over a wide pH range [16].

ZnO, a stable, opaque, and non-toxic powder, is used as a pigment in oil paints, watercolour paints, ceramic glazes, printing inks, glass colourants, cosmetics, pharmaceuticals, ointments, and UV as absorber [17]. As a white pigment, TiO_2 is mainly used in paints, food colouring, cosmetics, toothpaste, polymers, and other instances in which white colouration is requested. The reason why it is so widely used is that TiO_2 combines a high refractive index with a high degree of transparency in the visible region of the spectrum. Titanium oxide presents 2.73 for rutile and 2.55 for anatase (the most common TiO_2 structures) against the Zinc oxide 2.02. That is why this pigment is so used on the applications aforementioned [10, 18]. Paints use polymeric binders to fix the pigment and, when in contact with titania, the polymer may oxidise when exposed to sunlight. This effect is known as chalking and, in addition to the direct degrading effect of ultraviolet (UV) radiation, is accelerated by the photocatalytic activity of TiO_2, which also is enhanced by the high surface area of this material. However, being rutile less photoreactive than anatase, it is still sufficiently reactive to reduce exterior durability. This problem may be minimized if the surface is submitted to a treatment (with silica and/or alumina, for instance) [10, 18].

Due to the wide band gap (3.2 eV), anatase inhibits its use under visible light, the formulation of mixed-phase TiO_2, anatase and rutile, had been considered giving rise to a widely used pigment, TiO_2 P25. The latter presents better photocatalytic performance than any of the pure structures alone under visible light [19]. Also, because of TiO_2 wide band gap, ZnO has been proposed as an alternative photocatalyst. Although it presents the same band gap energy, it exhibits a higher absorption efficiency across a wide fraction of the solar spectrum when compared to TiO_2 [20].

2.2.2 Color Pigments

FeOOH is an example of inorganic yellow/orange pigment. This kind of pigment gives opaque films with good hiding features and high exterior durability. Its chemical and solvent resistance are excellent. As inorganic reds pigments, one has Fe_2O_3 as an example. It is a low chroma red with excellent properties and low cost. In contrast to iron oxide yellows, iron oxide reds are thermally stable and their excellent exterior durability makes the transparent grades suitable for use with aluminium in metallic automotive topcoats. Plus, transparent iron oxide is an excellent UV absorber and is used in transparent wood stains to protect the wood from photooxidation. [10].

2.2.3 Functional Pigments

Functional pigments have as a final goal to enhance or protect the surface in question - anti-corrosion in cars reduced flow resistance on the wings of aeroplanes, or they may be applied into electronic components to cancel out the electrical conductivity of the coated substrate.

As an example, ZnO which is used as fungicide [21], while Cu_2O is used as an anti-fouling coating in ships or, more recently, used to inactivate SARS-CoV-2, the virus that causes the disease COVID-19 [22].

Fe_2O_3 is another pigment that, among other shapes, may be lamellar or spherical. Despite being similar, their different shapes allow them to be used in different applications. Spherical-shaped pigments contribute to opacity, colour, abrasion resistance, or they may work as fillers, also aiding the flow out and gloss level, allowing formulation of glossy coatings. The lamellar shape retards the movement of water and other species inside the coating by forming a tortuous path for the molecules to go through. This barrier behaviour increases the lifespan of the surfaces [1]. Both shapes behaviour in the presence of fluids is depicted in Figure 2.1.
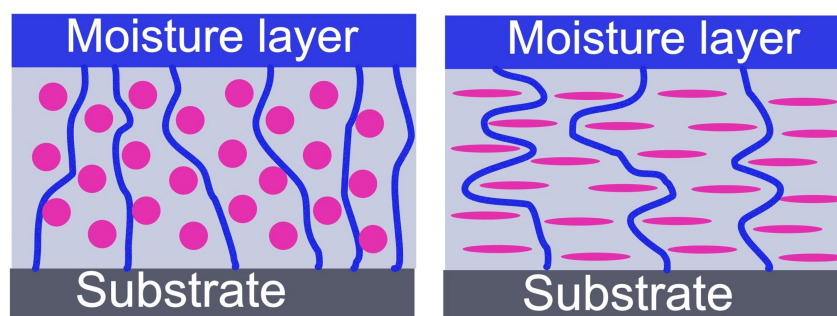
Figure 2.1: Barrier properties of shaped pigments: spherical (on the left) and lamellar (on the right) [1].

2.2.4 Nano-Pigments

Nano-pigments are pigments of very small particle sizes. Some authors consider nano-pigments every particle with diameters of less than 100 nm, but usually, the term is applied to diameters between 25 nm and 100 nm. Nanotechnology applications in coatings have aroused interest among the scientific community. That is due to their increasing availability, the wide range of accessible nanoparticles, the advancements in processes that can control nanosize coating structures, and the potential of nanotechnology to address many performance challenges of coatings [10].

Nanotechnology has helped to come up with solutions to improve the functional purposes of coatings. Compared to conventional pigments, nano-pigments present some advantages mainly due to the high surface area weight ratio. They may enhance resistance to scratch, abrasion, heat, radiation, and

swelling resistance, decrease water permeability, and increase hardness, weather ability, modulus, and strain-to-failure while maintaining toughness [10].

However, some drawbacks need to be addressed such as the tendency to agglomerate due to the reduced particle size [23], and the not so readily available techniques to characterize nanosize materials - Scanning Probe Microscopy (SPM) (e.g. Atomic Force Microscopy) and Scanning Electron Microscopy (SEM), Transmission Electron Microscopy (TEM), X-ray and neutron scattering [10]).

NPs seem to be a very good option for antimicrobial additives. Their size, which is similar to the size of the cells, facilitate the passage of particles through the membrane easily [24]. The embodiment of TiO_2 and ZnO NPs in paints also give anticorrosive, and self-cleaning purposes [25]. Silica, SiO_2, another example of a successful NP, may be used as filler in epoxy resins, enhancing the performance of wind turbine blades under superhydrophobic conditions. Generally adopted in hybrid organic/inorganic coatings, this type of coatings are transparent, show good adhesion, and enhance the scratch and abrasion resistance of a polymeric substrate when combined [26].

2.3 Photocatalysis

Photocatalysis is a process found in nature, as in photosynthesis, and mimicked by humans who developed it in a way which made possible the degradation of pollutants, H_2 production or even energy production of high-value chemicals [27].

The photocatalytic mechanism, to be explained in the following paragraphs, may be put as a scheme as follows - Figure 2.2.
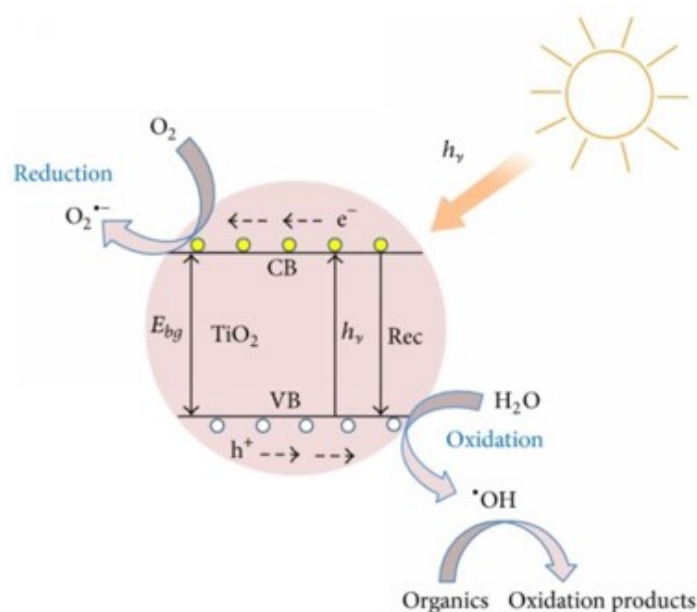
Figure 2.2: Scheme of the photocatalytic mechanism - TiO_2 [2].

The photocatalyst, which may also be referred to as semiconductor, consists of two bands - a valance band (VB) filled with electrons, and an empty band named conduction band (CB)- separated by a forbidden space called band gap. The band gap concerns the minimum amount of energy required to excite an electron from the valance to the conduction band. The absorption of light of suitable wavelengths by this photocatalyst promotes the electron migration from the valence band to the conduction band producing a pair electron/hole [28] - Equation 2.1.

$$Catalyst + h\upsilon \rightarrow e_{cb}{}^- + h_{vb}{}^+ \qquad (2.1)$$

The $e_{cb}{}^-$ are the electrons in the CB and $h_{vb}{}^+$ are the electron vacancy in the VB. This pair migrate to the catalyst surface where, being active, can perform reduction and oxidation reactions. These reactions must occur simultaneously so the photocatalyst operate sustainably and at the highest reaction rate possible. The $h_{vb}{}^+$ react with H_2O to produce $\cdot OH$ radicals - Equation 2.2. The $e_{cb}{}^-$ react with O_2 to produce $\cdot O_2^-$ radicals - Equation 2.3 [29].

$$H_2O + h_{vb}{}^+ \rightarrow \cdot OH + H^+ \qquad (2.2)$$

$$O_2 + e_{cb}{}^- \rightarrow \cdot OH + \cdot O_2^- \qquad (2.3)$$
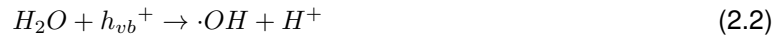
The migration of the pair electron/hole may follow one of the three distinct pathways as outlined below:

- Semiconductor donates electron to reduce an electron acceptor adsorbate;

- Holes can migrate to the surface where an electron from a donor species can combine with the hole oxidizing the donor adsorbate;

- Recombination of the electron/hole on the surface of the semiconductor or even inside the semi-conductor.

The recombination of electron/hole pairs is one of the main causes for the low yield of photocatalytic processes since the recombination of charges is more favourable than their diffusion to the surface. Some actions need to be taken to prevent this event. To do so, the surface of a semiconductor is modified in diverse ways - using sacrificial reagents, adding co-catalyst particles on the semiconductor's surface, or improving the crystallinity of the photocatalysts [30].

2.4 Photocatalytic Coatings Applications

Some pigments give coatings some appealing features, such as photocatalytic properties.

Photocatalytic coatings may favour the degradation of pollutants, give self-cleaning properties or even give anti-bacterial properties to the coated materials. It may be applied on the top layers of concrete, paint, or mortar, regarding building facades, or even on the top of glass, metals or polymers [31].

The Figure 2.3 gives an overview of how all these applications work.
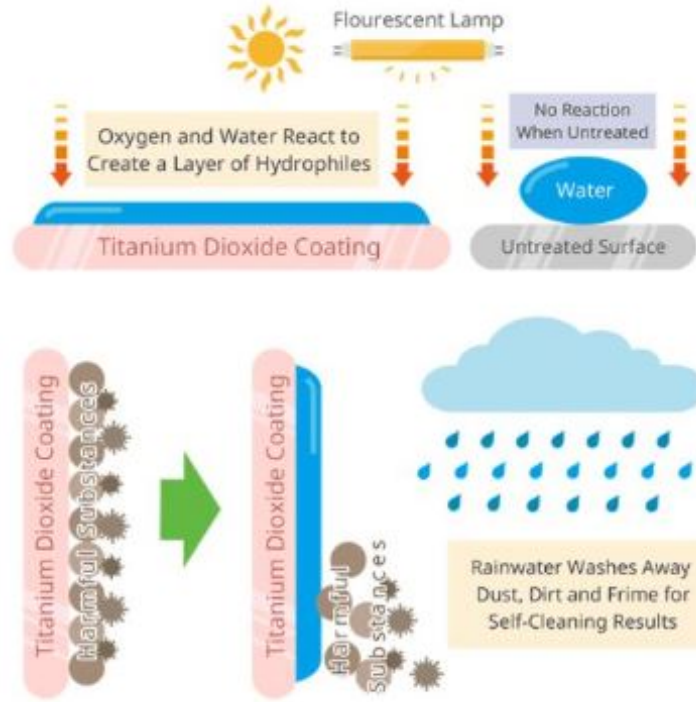
Figure 2.3: An illustrative example of photocatalytic coating applications [3].

2.4.1 Degradation of Pollutants

Indoor and outdoor air quality is a parameter related to health and environmental concerns. Some efforts have been made to control and mitigate this problem [32].

Indoor air quality is, most of the time, worse than outdoor air quality. That may be explained by the activities developed inside and the poor air exchanging rate conditions. Combustion processes release high NOx levels in the indoor air (gas stoves, gas ranges, and burning candles and incenses) [33]. Concerning outdoor air pollutants, the harmful effects of vehicle emissions, such as NOx, contribute to environmental issues, like the formation of tropospheric ozone and urban smog, as well as it may provoke acute respiratory tract infections and cardiovascular diseases [34]. Photocatalytic remediation technology is considered a promising way to tackle these problems.

TiO_2 photocatalytic NPs are considered a promising way to mitigate the harmful effects of vehicle emissions. When applied as road coating and in the presence of light, these photocatalysts may trap and decompose those air pollutants [35]. Indoors, instead of being diluted or disposed, air pollutants may be eliminated using PC reactions [36], eliminating volatile organic compounds (VOC) and nitrogen oxides (NOx) [37]. TiO_2 photocatalytic NPs are particles that degrade NOx pollutants. NO_2 is adsorbed onto the semiconductor's surface, and according to Langmuir-Hinshelwood kinetic mechanism, the reaction with hydroxyl radicals occur.

$$NO_2 + \cdot OH \rightarrow HNO_3 \tag{2.4}$$

$$NO_2 + O_2^- (+H^+) \rightarrow NO_2^- (HONO) + O_2 \tag{2.5}$$
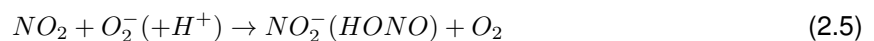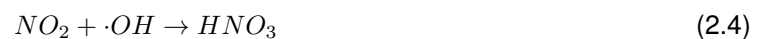
An then, the PC reaction occur.

$$2NO_2 + H_2O \overset{+h\nu, TiO_2}{\rightarrow} HONO + HNO_3 \tag{2.6}$$

8

Being the HONO the most important source of OH radicals.

2.4.2 Self-cleaning

The self-cleaning function of a coating proved to be a breakthrough in everyday life. Merging photocatalytic NPs with coatings originated this very successful kind of coatings that are usually applied in glass, cement or even marble surfaces. However, there are some challenges to be addressed. Photocatalytic NPs may degrade the binders on the organic coatings, so photocatalytic clearcoat cast onto traditional organic coatings needs improvement.

Having TiO_2 as an example, the shift in its wettability and formation of a highly hydrophilic surface state contributes to the self-cleaning characteristic of a surface. The phenomenon is known as photoinduced super hydrophilicity by UV light irradiation. The reduction of Ti_4^+ to Ti_3^+ by electrons and simultaneous hole trapping at lattice sites reduces the bond strength between reduced titanium and the closest O_2. The O_2 is removed and the closest water molecule is adsorbed. In short, contaminants are first photo-mineralized, at least in part, and subsequently washed away by water, which spreads below them in tight contact with the TiO_2 surface [38]. Figure 2.4 illustrates the hydrophilicity phenomenon behind the self-cleaning effect.
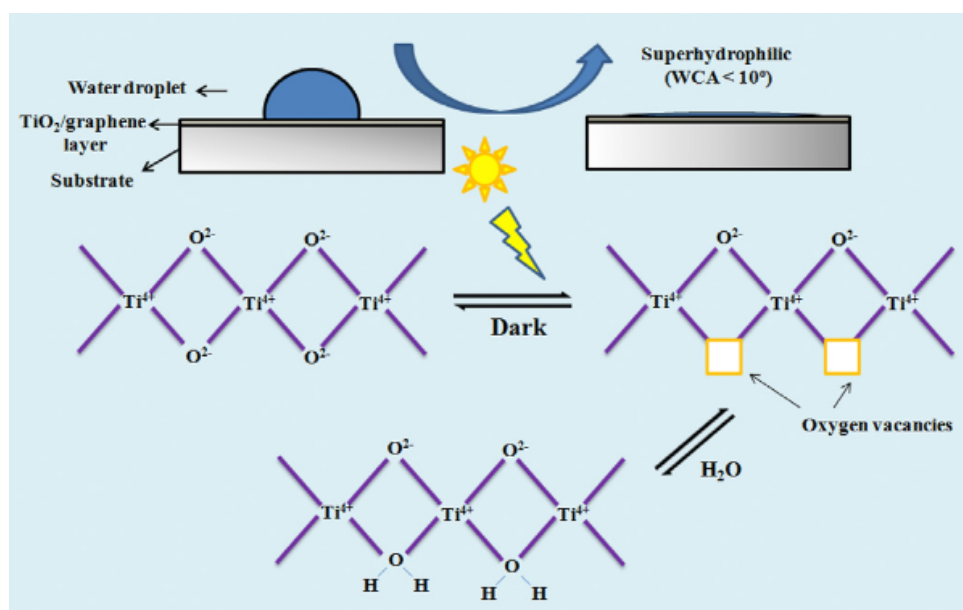
Figure 2.4: The mechanism of photoinduced superhydrophilicity in self-cleaning materials and coatings [**?**]

Although usually undesirable, self-cleaning white house paints are deliberately formulated with anatase TiO_2, which fails more quickly on outdoor exposure by chalking, so they chalk readily. When the surface of the film erodes, dirt accumulation is also removed, so that the paint surface stays whiter [10].

2.4.3 Anti-bacterial Properties

Surfaces may evolve into a favourable environment for microorganisms to grow and colonize. The TiO_2 and ZnO based nano-photocatalytic coatings have been applied in ceilings, interior and exterior walls to control the spread or to eliminate organic compounds, bacteria, mould, and viruses. This ability to mediate the destruction of bacteria, viruses and other biological materials is also known as photo-sterilization. The radicals generated by the PC nanocoatings attack bacteria or viruses inhibiting DNA

clonal processing and destroying the coenzymes and enzymes. The reproduction of bacteria and moulds is stopped, inhibiting bacteria growth and preventing virus DNA from multiplicating [**?**].

2.5 Photocatalytic Pigments

2.5.1 TiO$_2$-based Pigments

It was the 1970s when Fujishima and Honda [39], as well as Wrighton et al. [40], discovered the photocatalytic splitting of water in a titanium oxide sample. That discovery was the trigger to promising applications to be created in various fields including solar energy, green chemistry, and environmental remediation [41] [42]. Today, Titanium dioxide is one of the most widely studied polymorphic compounds in the metal oxide semiconductors group. All because it is inexpensive, highly photoactive and easily synthesized and handled [43] [44].

The three main TiO$_2$ crystal structures are anatase, brookite, and rutile. Anatase has a higher band gap value, a higher surface area and porosity, and a higher PC activity when compared to the other aforementioned structures of TiO$_2$. However, applications using anatase have some disadvantages such as low quantum performance and requiring UV light to be active [45]. Even though anatase is considered to be more active than rutile under UV light, rutile shows better photoabsorption property in visible light - anatase phase has a higher band gap value (3.2 eV) than rutile (3.0 eV). Rutile also revealed an excellent refractive index, high dielectric constant, higher hiding power and superior chemical stability. However, for nanosized structures, in the order of 10–20 nm, anatase display a more stable morphology than rutile [43] [46]. In general, rutile is universally used as a white pigment in coatings, mainly due to its high hiding power (i.e. ability to provide opacity). It is preferred over anatase due to this and also to the lower PC activity (which may be an advantage depending on the application).

A representative TiO$_2$ nanoparticle product is Evonik AEROXIDE® TiO$_2$ P-25 (denoted as P25) manufactured via a proprietary Aerosil process, namely, TiCl$_4$ vapor-fed flame pyrolysis process. This mixture of anatase and rutile phases (80:20) unveiled a synergistic effect where the inactive rutile enhances the PC activity of anatase [47]. It has high chemical purity, relatively broad light absorption, low aggregation, excellent dispersion especially in liquid media, and high quantum efficiency and photocatalytic activity for various photocatalytic reactions. Its so good PC performance may be explained by the improvement of the magnitude of the space-charge potential due to the efficient charge carrier separation. This improvement is due to a change in the design by constructing a photocatalyst combining two different ones [48]. That results in a much higher PC activity than that of sole-phase TiO$_2$, either anatase or rutile [47].

2.5.2 Non-TiO$_2$-based Pigments

TiO$_2$-based pigments present some disadvantages. Even though their good activity under UV light, they show poor activity under visible light (sunlight). Because the UV component accounts for only around 8% of the visible light, not being able to uptake Vis light (accounting for around 50%) results in poor use of the sunlight. Also, due to the recent suspicion on TiO$_2$ causing health-related problems, there is a need to find other alternatives to this pigment. A pigment that also needs improvement of its own photocatalytic performance. Few of the alternative pigments in study nowadays will be covered here.

TiO$_2$-based pigments are not visible-light-responsive photocatalysts. Studies have been carried out to come up with efficient uptake of visible-light energy solutions. Cu$_2$O has been known as an alternative photocatalyst (2.0–2.3 eV). Also, as a nano-sized photocatalyst, electron/hole recombination is avoided and active and efficient photocatalysts are produced. It occurs because of the decrease in particle size

as well as an increase in specific surface area [49]. ZnO nanostructures are prominent photocatalyst candidates [50] as they are low-cost, non-toxic and more light absorbent efficient across a large fraction of the solar spectrum compared to TiO_2. FeOOH, an earth-abundant material, is a non-toxic and inexpensive small electronic band gap photoactive material capable of using visible light to drive redox reactions. These pigments also have outstanding chemical and physical properties, including environmental compatibility, high photostability, and excellent visible light absorption [51]. Fe_2O_3, considered an important material for degradation of numerous dyes and organic contaminants, its tolerable band gap, wide harvesting of visible light, good stability and recyclability make this pigment a good TiO_2 alternative [52].

Table 2.1: Samples and each band gap value.

Sample	Band Gap
TiO_2 P25	3.21
TiO_2 rutile	3.00
TiO_2 anatase	3.20
ZnO	3.25
Fe_2O_3 lamellar	1.97
Fe_2O_3 spherical	1.97
FeOOH	2.15
Cu_2O	2.35

2.6 Photocatalytic Coatings Challenges

The general photocatalytic challenges to tackle are:

- **Photocatalyst deactivation**
  The blockage of the photocatalytic active sites by partially oxidized intermediates hinders the PC reaction [53].

- **Catalyst photo-oxidation**
  Formed oxidizing radicals oxidize the catalyst itself instead of catalyzing a reaction such as the photodegradation of a pollutant [54].

- **Electron/hole recombination**
  Photogenerated charge carriers recombination reduces quantum efficiency. When recombination occurs, the electrons revert to the valence band, prompting no reaction with the adsorbed species dissipating the energy as light or heat. Impurities or defects may contribute to this process which may take place on the surface or in the bulk [53]. Several approaches have been suggested to improve recombination time. The addition of metallic nanoparticles or metallic ions (Ag, Au, Pt, Pd, Fe, Cu) has been considered a way out once they increase the recombination time by creating traps within the band gap. Having TiO_2 as example, the combination of semiconductors is also a solution (TiO_2/ZnO, TiO_2/CdS, TiO_2/Bi_2S_3, TiO_2/ZrO2). To reduce the band gap, metallic ions (Cu, Fe), dye molecules (porphyrins) and non-metallic elements (N, P, S, F) have been considered [12].

Specifically, photocatalytic coatings have plus other challenges to take on, such as:

- **Incorporation PC material/organic matrix**
  Some PC materials may degrade the film-forming agent at the time of the coating formation. Also,

PC powers may see their photocatalytic performance decreasing thanks to the components that formulate the coating. That is due to restrict access of light and reactants to the PC species resulting in inefficient utilization of light and reactants [55]

- **Binder stability**
  The photocatalyst may degrade the organic components of the film. It is that initial photo-degradation that plays the active role of the PC coatings. Because the binder is partially degraded, that allows light and reactants to access the photocatalyst, rendering the coating surface photocatalytically active [56] [57].

- **Poor dispersion of nanoparticles**
  This phenomenon happens due to the strong tendency of the pigments to agglomerate because of the high surface energy, which enables this major benefit to occur. To take on this issue, there are some deserve mentioning approaches. Surface treatment of the pigments in *situ* polymerization in the presence of the pigments, special pigment dispersants, and ultrasonic dispersion (the latter adopted on this project) [10].

- **Toxicity**
  The raising suspicion about the impact on human health from the raw materials has triggered the European Union's attention resulting in an intent to seek uniformity on the regulation in the EU. Besides the European Center for Ecotoxicology of Chemicals (ECETOC), also the US Environmental Protection Agency (EPA) have published the results which state the peril of dealing with this type of materials [10]. TiO_2 in power form was classified as suspected of causing cancer in humans by inhalation by - EU statement, 2020 [14]. Even though there is no consensus on the carcinogenic effect caused by the pigment, there is a common concern in finding new feasible human-health-friendly, as well as environmentally-friendly, options [58].

Having as main driving forces the poor activity under Vis light and the recently discovered toxicity of TiO_2-based photocatalysts, this project will focus on the feasibility of each non-TiO_2-based as alternatives to the TiO_2-based alternatives widely available on the market nowadays.

Chapter 3

Experimental Methodology

In this chapter, the experimental methodology, the physical/chemical characterization techniques and the catalytic test protocol were described.

3.1 Materials

After evaluating the state-of-the-art, it could be concluded that several pigments were already in use in Coatings Industry whose potential as photocatalyst is under investigation. Here, a benchmark approach was adopted to evaluate the photocatalytic potential of a set of elected pigments. Those are TiO_2-based, Ti_2O anatase, Ti_2O rutile, Ti_2O P25, having the P25 as a state-of-the-art pigment, and also non-TiO_2-based, Fe_2O_3 lamellar, Fe_2O_3 spherical, Cu_2O, ZnO, and FeOOH. The Ti_2O-based PC materials are all white-pigments, as well as the ZnO. All the other non-Ti_2O-based ones are color - Section 2.2. The Fe_2O_3 lamellar and spherical are pigments which, besides having a different shape, also have a different structure - Section 4.1. Among these, the Ti_2O-based ones were elected as a reference once these are the most studied ones.

A summary of the characteristics of the samples in study provided by the supplier can be consulted in Table 3.1.

Worth-mentioning that, apart from Ti_2O anatase and Ti_2O P25, all the pigments were provided by the Coatings Science and Technology Centre (CoaST) and shipped to Portugal.

Table 3.1: List of the samples used. Purity and supplier.

Sample	Supplier	Commercial Reference	Purity (%)
TiO_2 P25	Sigam-Aldrich	Aeroxide P25	99.5
TiO_2 rutile	Chemours Company	R-101	97.0
TiO_2 anatase	Merk	-	99.0
ZnO	EverZinc	ZnO Indirect	99.9
Fe_2O_3 lamellar	Promindsa	Micronox R01	76-95
Fe_2O_3 spherical	Promindsa	Micronox R110	76-95
FeOOH	Lanxess	Bayferrox 943	99.4
Cu_2O	Nordox	Nordox Cuprous Oxide	99.0

The photocatalytic properties of the compounds that make up these pigments have been reported elsewhere, either as stand-alone or mixed photocatalysts [43, 45–52].

To evaluate the performance of each sample, the ability to degrade a dye under the influence of light was studied. Sigma-Aldrich methylene blue (97% purity, dry basis) was chosen as a dye. Sigma-Aldrich mentions the presence of water in methylene blue (MB). To investigate the amount of water in it a thermogravimetric analysis (TGA) was performed. The MB was revealed to be 10% hydrated. That 10% H_2O were considered when weighting every amount of MB. Distilled water (DW) served as a dispersion medium.

3.2 Characterization Techniques

The characterization of the samples was done resorting to two techniques, those providing comprehensive information on the physicochemical, structural, and morphological properties of the samples. Four characterization techniques were used - X-ray Powder Diffraction (XRD), UV-Vis Diffuse Reflectance Spectroscopy (DRS), Dynamic Light Scattering (DLS), and N_2 - sorption.

3.2.1 X-ray Powder Diffraction (XRD)

The method consists of X-ray beams that hit the powder's surface and are diffracted into specific directions depending on the sample's crystallographic characteristics. The angles and the intensities of the diffracted beams are measured and collected giving rise to a pattern called diffractogram. The acquired diffractogram was then confronted with the database's references until a structure corresponding to a particular crystalline structure is found. This way, the type of structure, as well as the crystallite size of the powder samples, are identified [59].

This technique provides information about the phase of a crystalline material, determines the cell dimensions, and measures the purity of the sample. The X-ray powder diffraction (XRD) measurements were carried out using D8 Advance diffractometer from Bruker, Figure 3.2, equipped with a Cu lamp (CuKα = 1.5406 Å), a 1D LynxEye detector and a Ni filter. Experiments were performed from 5 º to 80 º (2 Theta) with a step size of 0.05 º and a step time of 1 s. Results were analyzed with TOPAS software (version 5.2) from Bruker.
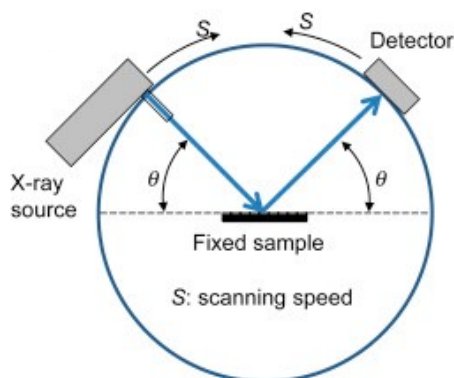
Figure 3.1: Powder X-ray diffraction scheme [4].

Figure 3.2: Powder X-ray diffractometer from BRUKER [5].

Preformed by the software, the crystallite size (L) of the powders was calculated by measuring the full width at half maximum of all the reflections based on Debye-Scherrer's formula given by Equation 3.1 [46].

$$L = \frac{k\lambda}{\beta cos\Theta} \tag{3.1}$$

Being *k* a dimensionless shape factor, with a value close to unity that varies with the actual shape of the crystallite; λ the X-ray wavelength; β the line width at half maximum height (FWHM) of the peak, and θ the Bragg's diffraction angle.

Figure 3.3 is an example of a diffractogram aquired by this technique.

Figure 3.3: Example of a diffractogram obtained (ZnO) and comparison with zincite (COD 9004180) structure found in COD database.

3.2.2 UV-Vis Diffuse Reflectance Spectroscopy (DRS)

Diffuse reflection spectroscopy (DRS) is an analytical non-evasive technique that can be used to quantify the optical absorption and scattering properties of a medium, which in turn can provid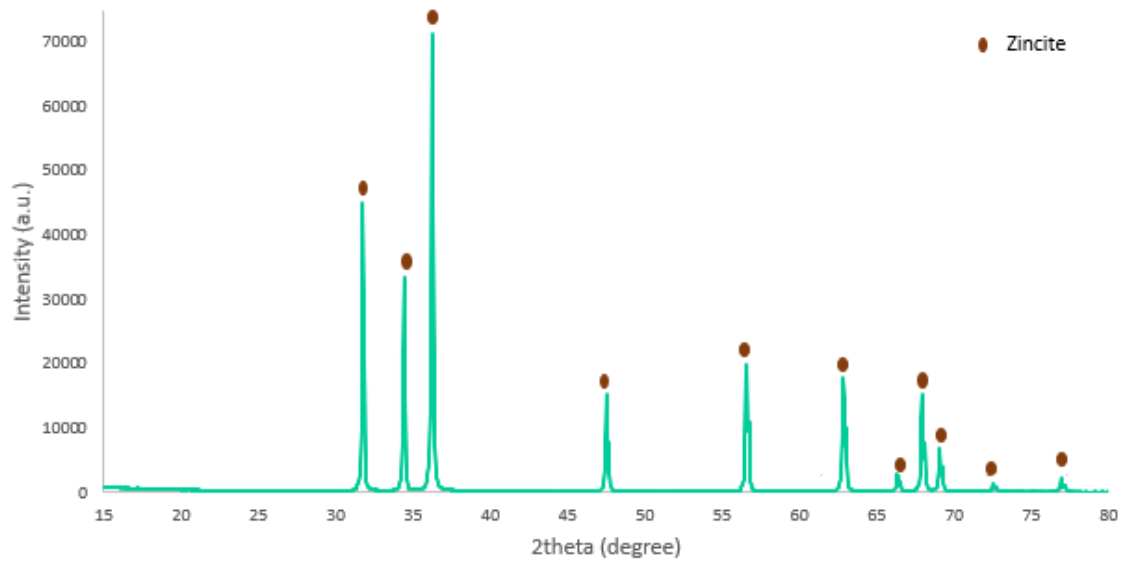e important functional and/or structural parameters relevant to the sample in study. It uses ultraviolet (UV), visible, or infrared (IR) light as a probing medium. Experimentally, a beam of light passes through the medium of interest using a fibre-optical conduit and the detected emitted signal from the surface using another optical fibre is fed into a spectrometer. The detected signal is sensitive to the distribution of the optical properties of the medium [60].

The UV-Vis spectra of each pigment were obtained using the Cary 5000 spectrophotometer from Varian, Figure 3.4, equipped with a Praying mantis accessory for DRS measurements. The information was recorded sweeping wavelengths from 200 up to 2500 nm. The scans were obtained with a spectral bandwidth of 4 nm, a scan rate of 600 nm/min, and a data interval of 1 nm.

Figure 3.4: Spectrophotometer Cary 5000 from VARIAN and the support used for powder samples [6].

Figure 3.5 is an example of what is obtained resorting to this technique.
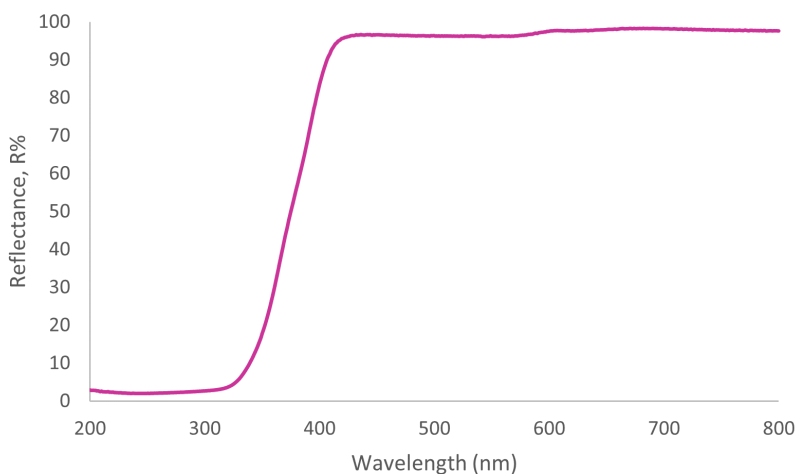

Figure 3.5: Example of a reflectance spectrum obtained by the DRS technique (TiO$_2$ P25).

Resorting to the Kubelka-Munk theory - which covers the behaviour of light flux through homogeneous isotropic media - it is possible to relate the diffuse reflected light to the absorption coefficient, K [61]. The fundamental equation goes as follows.

$$F(R_{inf}) = \frac{K}{S} = \frac{(1 - R_{inf})^2}{2R_{inf}} \tag{3.2}$$

Being S the backscattering coefficient and R_{inf} the remission fraction of an infinitely thick layer. Both S and K are defined by the corresponding thickness of the layer. It is assumed that S changes negligibly within the wavelength region of electronic absorption being the Kubelka-Munk function solely dependent on K. This assumption facilitates the calculations in a way that the absorption, α, can be related to K using the Tauc relation [61–63].

$$F(R_{inf}) \cdot hv)^{\frac{1}{n}} \sim (\alpha \cdot hv)^{\frac{1}{n}} \tag{3.3}$$

Being h the Planck's constant, v the speed of light, α the absorption coefficient, n the type of electronic transition, and Eg the optical band gap energy.

For each semiconductor, there is a correspondent band gap value. An electron may shift from the lowest-energy state in the VB to the highest-energy state in the CB directly or by changing its crystal momentum (k-vector) in the Brillouin zone (the smallest volume entirely enclosed by planes) [7]. If the crystal momentum of the electron and the holes is different, the transition is indirect. If not, the transition is direct. Figure 3.6 represents the direct and indirect transition. Unlike the Figure 2.2 where the crystal momentum was not taken into account.
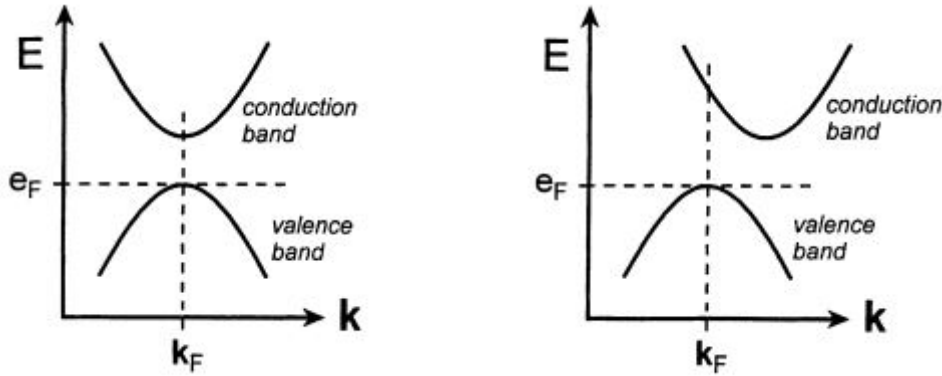
Figure 3.6: Schematic representations of electronic band structures near the Fermi level for a solid - direct transition on the left, and the indirect transition on the right. e_F is the Fermi level having the Fermi wave vector, k_F (k-vetor) [7].

The type of electronic transition, n, may assume different values as the Table 3.2 depicts.

Table 3.2: Transition types and the correspondent value.

Transition Type	n
Direct, allowed	1/2
Direct, forbidden	3/2
Indirect, allowed	2
Indirect, forbidden	3

By plotting the modified diffuse reflectance, $F(R_{inf})$, versus the photon energy, hv, the optical band gap energy, Eg, is the value which corresponds to the intersection of the tangent line with the plot with

the xx axis [61]. The tangent line should be drawn on the far left most absorption curve edge as depicted in Figure 3.7.

Figure 3.7: Example of a Tauc Plot obtained resorting to Kubelka-Munk equation (TiO_2 P25).
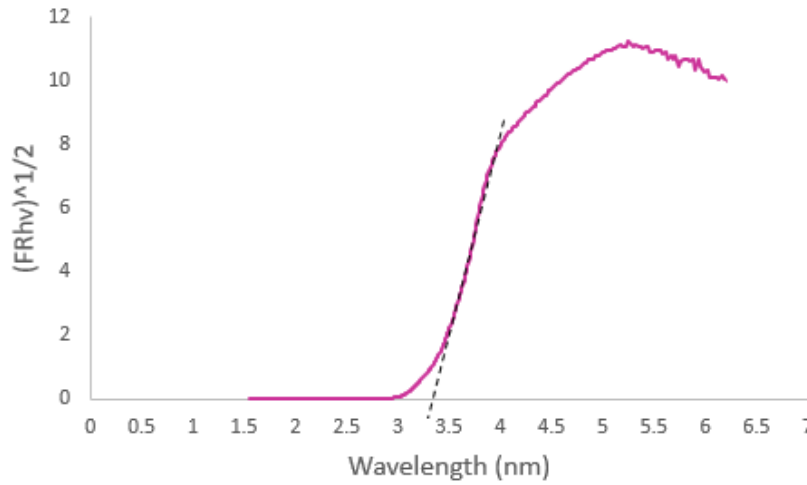
When there are two consecutive curves in the Tauc Plot, another approach is adopted. Two tangent lines are drawn and their intersection gives out the band gap value [62]. Figure 3.8 illustrates this second method.
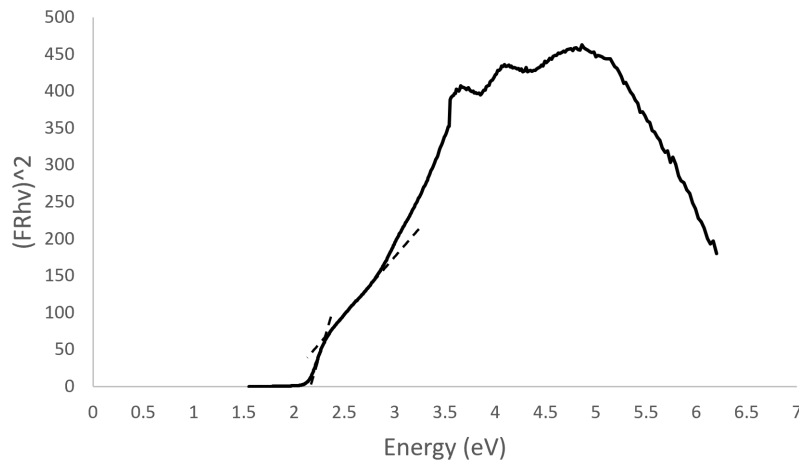
Figure 3.8: Example of a Tauc Plot obtained with the second method (Fe_2O_3 lamellar).

3.2.3 Dynamic Light Scattering (DLS)

The technique can be used to determine the size distribution profile of small particles in suspension. The intensity of the light scattered is measured as a laser beam passes through a dispersed particulate sample. This data is then analyzed to calculate the size of the particles that created the scattering pattern [64].

This technique was performed in a partner university, Instituto Superior de Engenharia de Lisboa (ISEL), by Manuel Vargastina. All the pigments, apart from the Cu_2O, were dispersed in water. Due to its hydrophobic behavior, the Cu_2O powder was dispersed in isopropanol. However, the results were not obtained under the same experimental conditions. Because not all samples were sonicated, some may have agglomerated what made the comparison process difficult. Due to the lack of time, the sample

preparation was not optimized. Regarding the dispersibility in water, a parallel experiment was performed
- check Appendix **??**

3.2.4   N$_2$-sorption Studies

N$_2$ adsorption/desorption isotherms (volume of N$_2$ adsorbed as a function of N$_2$ relative pressure)
were recorded using Micromeritics ASAP 2010 apparatus after a pretreatment stage consisting of heat-
ing the samples up to 500ºC. Among all the existing models, the BET model is the most used model.
The BET applies to solids with multilayer adsorption and is used to compute the specific surface area.
Probing gases that do not chemically react with material surfaces such as N$_2$ are used ones to quantify
specific surface area.

First, the results are linearized according to Equation 3.4, where P/P_0 corresponds to the relative
pressure, V_A to the adsorbed volume of N$_2$ at pressure P, V_M to the volume of the monolayer, c is the
enthalpy of adsorption for the first layer. The monolayer volume (V_M) can then be estimated and used
to compute the BET area according to Equation 3.5 [65].

$$\frac{\frac{P}{P_0}}{V_A.(1 - \frac{P}{P_0})} = \frac{1}{V_M.c} + \frac{c - 1}{V_M.cP_0} \tag{3.4}$$

$$S_{BET} = \frac{V_M \sigma N_A}{mV_0} \tag{3.5}$$

This technique was performed for only one sample, Cu$_2$O. The results obtained were not conclusive
because of the so small crystallite size (33 nm).

3.3   Photocatalytic Performance Evaluation

To evaluate the photocatalytic performance of all the powders under the influence of light, the degra-
dation of a dye was carried out in a photochemical reactor. MB was the dye chosen and two types of
light sources were used. The photolysis experiment to evaluate the MB degradation under each light
source, and the study of adsorption-desorption equilibrium between the dye and the powder was also
evaluated.

Before describing these two techniques, the introduction of the MB, as well as the clarification of why
this degrading dye was adopted, needs to be addressed.

3.3.1   Methylene Blue (MB)

Methylene blue is a heterocyclic aromatic chemical compound applied in different fields, such as
biology and chemistry. It has a characteristic deep blue color in the oxidized state, but the reduced form,
leucomethylene blue (LMB), is colorless - Figure 3.9 [66].
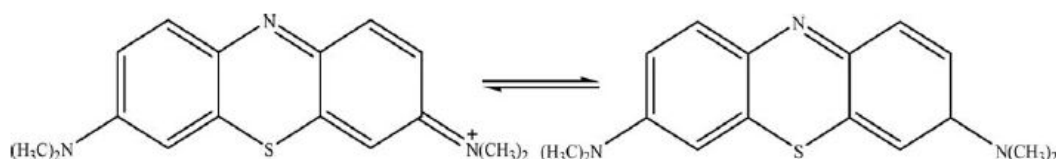
Figure 3.9: MB (left) and Leucomethylene Blue (right) organic structures.

Figure 3.10 shows the photocatalytic degradation pathway of MB.
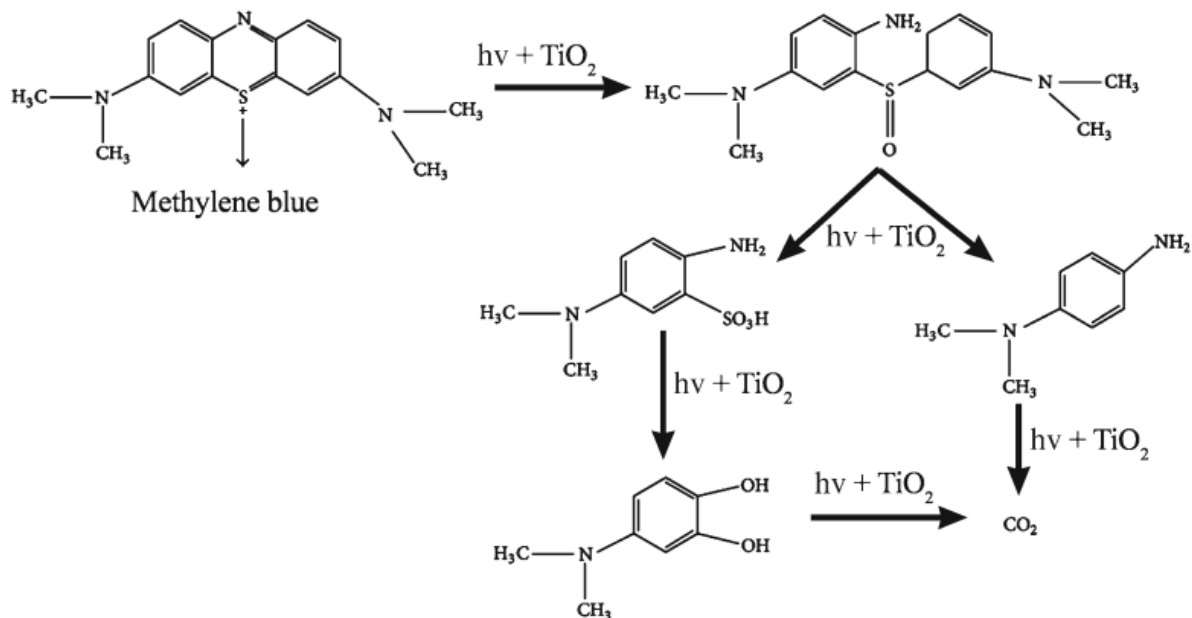
Figure 3.10: MB photodegradation reaction pathway [8].

Under the influence of light *hv*, and in the presence of a photocatalyst (i.e TiO_2), MB is reduced to LMB which may continuously be degraded in the presence of light and a photocatalyst.

3.3.2 Reactor Set-up

The Figure 3.11 shows the reactor available at Instituto Superior Técnico Instituto Superior Técnico (IST).

Figure 3.11: Photochemical reactor with changeable light bulbs.

This setup comprises six light bulbs placed vertically so the light may irradiate the Erlenmeyer evenly. In the center of the apparatus, an Erlenmeyer (250 mL) with a lid on and containing the slurry is placed in th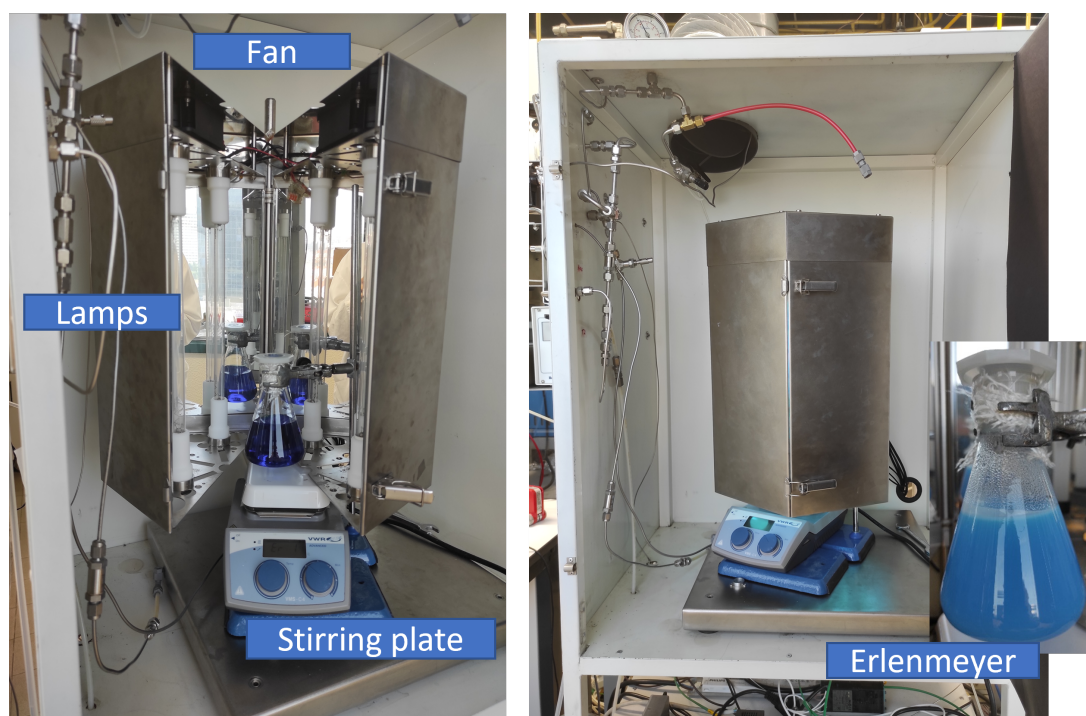e middle (400 mg/L of the sample; 10 mg/L of MB). Having a stirring magnet inside, the slurry is magnetically agitated by the stirring plate on the bottom at 2000 rpm. There is also a fan that maintains the temperature inside the reactor during the experiment at room temperature - between 27ºC and 31ºC.

Source of light

The energy irradiated from the Sun provides light and heat indispensable to life on Earth. There are three different bands along the spectrum: ultraviolet (UV), visible, and infrared (IR). Each band accounts for approximately 8%, 50%, and 42%, respectively

The UV component can be divided into three other bands depending on the intensity. The most energetic, UV-C (100-280 nm), the UV-B (280-320 nm), and the less energetic UV-A (320-400 nm). Visible range spans 380 to 700 nm. Infrared range spans 700 nm to 1,000,000 nm (1 mm), and may also be divided into A (700-1,400 nm), B (1,400-3,000 nm), and C (3,000-1 mm) category.

The experiments were carried out using two types of light sources. All the information about those light bulbs are summarized in Table 3.3 and Figures 3.17a and 3.17b.

Table 3.3: Model and characteristics of the source of light.

Name	Philips	Exo-Terra
Model	TUV 4P SE UNP/32	Reptil Glo 10.0 T8
Power (W)	16*6	14*6
Light Source	UV-C (250 nm)	UV + Visible
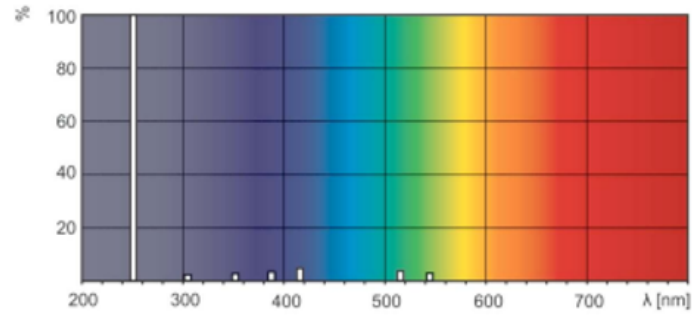
(a) Philips light bulb. Germicide bulb (UV-C light).
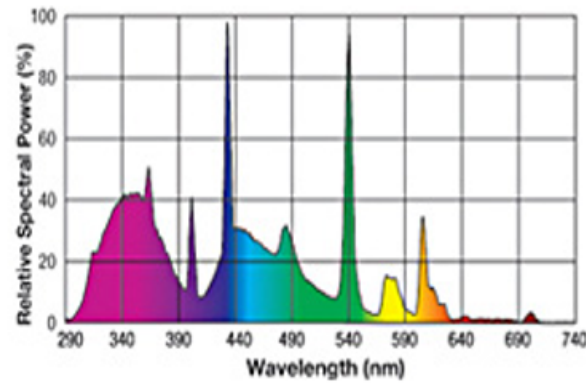
(b) Exo-Terra light bulb. Solar mimic light bulb (UV-Visible light).

Figure 3.12: Spectra of the light sources used.

Figure 3.13: The solar spectra on the sea level and outside the atmosphere.

As compiled in Table 3.3, the Philips bulb has an expressive UV-C light component. That is why it is mainly used for germicidal purposes. The Exo-Terra one mimics the Sun, and that is why it is so used in terrariums, as it may be confirmed with the Figure 3.13.

22

3.3.3 Calibration Curve

A calibration curve is a regression model used to predict the unknown concentrations of analytes of interest based on the response of the instru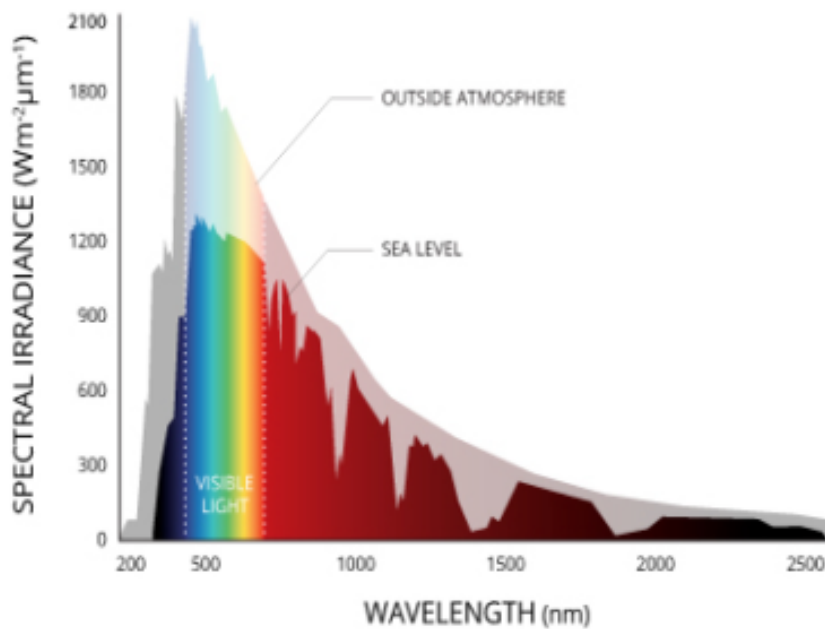ment to the known standards. It is also a model that enables the user to be sure about the reliability of the data obtained. To build the calibration curve 100 mL solutions were prepared (2 ppm, 4 ppm, 6 ppm, 8 ppm, 10 ppm, 10 ppm, 12 ppm, 14 ppm, 16 ppm,18 ppm, and 20 ppm) and magnetically stirred for 15 min. The absorbance spectrum of MB was plotted for each solution and two absorption peaks stood out - λ = 292 nm and λ = 664 nm - Figure 3.14.
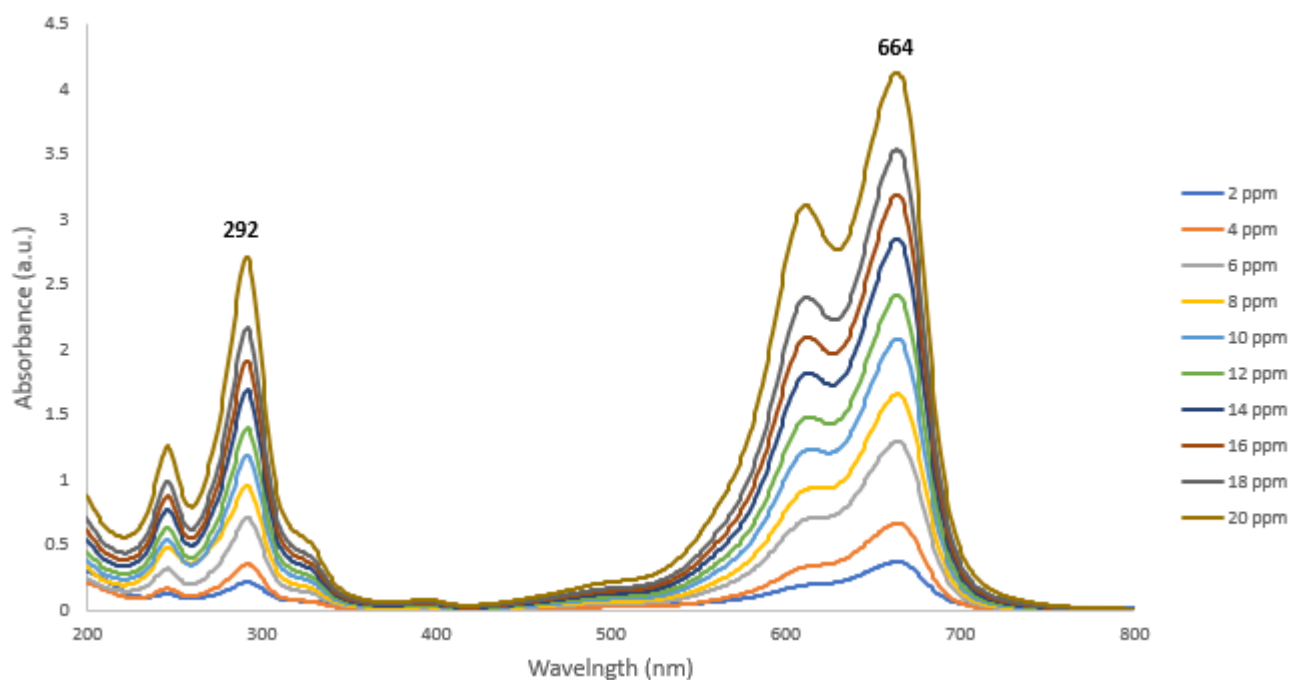

Figure 3.14: MB absorbance for different concentration - calibration curve.

The regression was plotted for λ = 664 nm because the light absorbance is much more significant at 664 nm than at 292 nm - Figure 3.15.
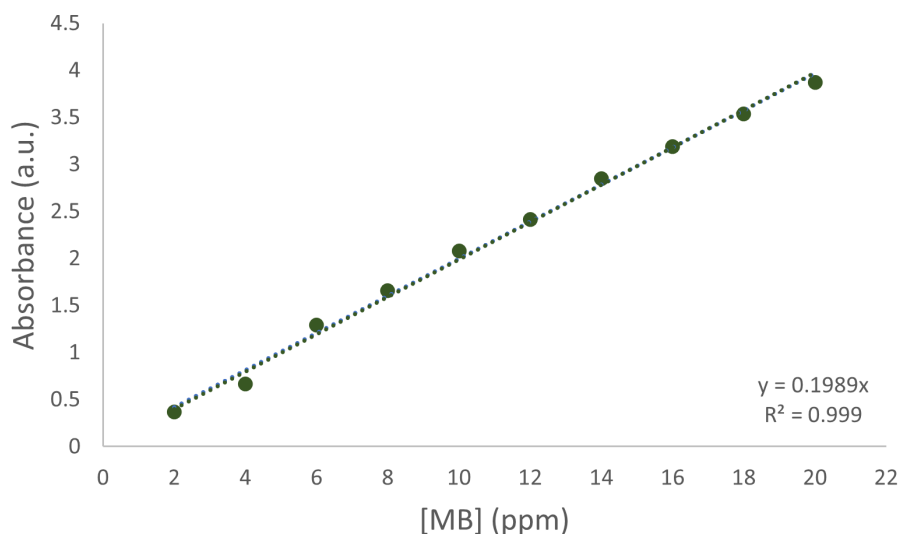

Figure 3.15: MB calibration curve for 664 nm.

3.3.4 Pre-photodegradation Tests

Photolysis

Photolysis is the decomposition or separation of molecules by the action of light. In order to check if the studied dye was active when irradiated, a solution of MB was prepared and left under its action for 3h. After building the calibration curve and going through some literature, two concentrations of MB were chosen - 10 mg/L and 20 mg/L and the protocol settled. A 250 mL Erlenmeyer was firstly sonicated for 5 min and then magnetically stirred in the dark for 1 h to attain homogeneity. Right before the UV-C light was turned on, a sample was withdrawn and its absorbance measured on a spectrophotometer. Right after, the light was turned and a sample was withdrawn every 20 min. Every experiment stopped after three hours.

The MB concentrations showed a good absorbance extent, which, being less sensitive to changes, would facilitate better results. Both concentrations proved to be very stable (10 mg/L 5% more degraded after 3 h) over time under UV-C. Figure 3.16 corroborates MB 10 mg/L stability under UV-C light.
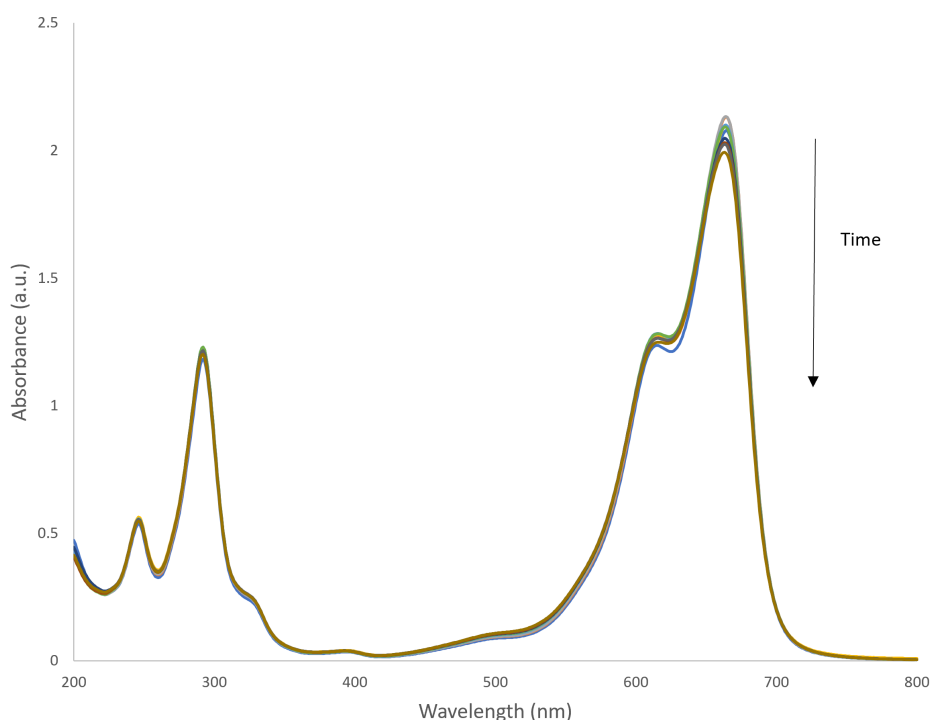
Figure 3.16: MB (10 mg/L) degradation under UV-C light.

Because the behaviour was roughly the same - 10 mg/L degraded 5% and 20 mg/L degraded 1% - the 10 mg/L was chosen over the 20 mg/L concentration, mainly because it is a concentration typically used in similar works.

When the light bulbs were swapped for UV-Vis light bulbs, the same protocol was followed for MB 10 mg/L where 4% of MB was degraded. In both scenarios, the results showed that these light sources do not contribute to dye degradation alone. Figures 3.17a and 3.17b show how the MB absorption spectrum for the UV-C and UV-Vis light bulb spectrum do not overlap each source of light spectrum - check Figures 3.17a and 3.17b, respectively . That corroborates the fact why MB does not suffer photolysis.
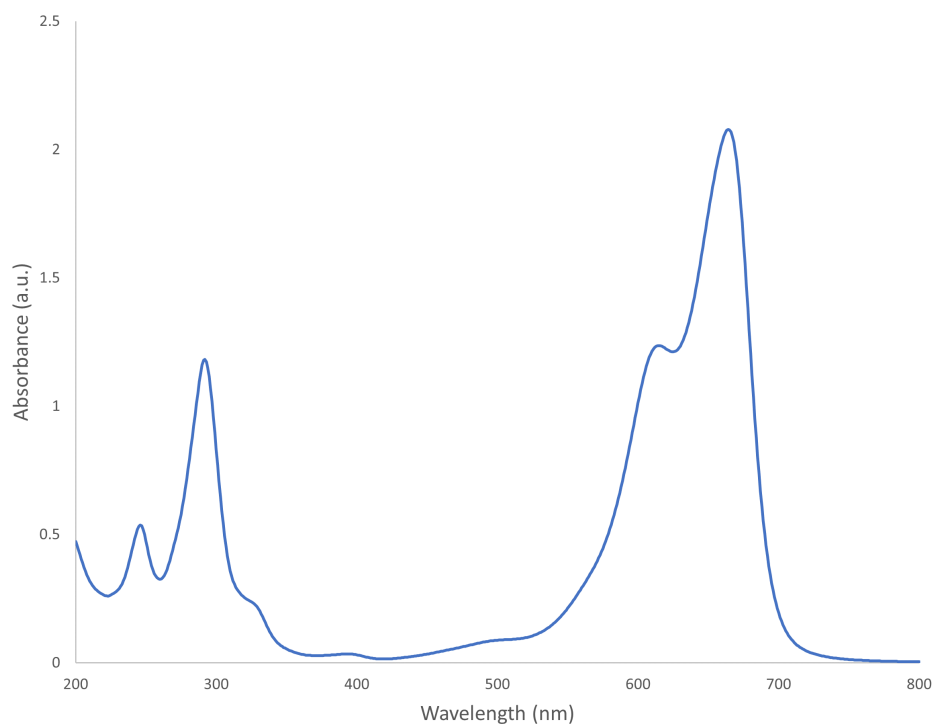
(a) MB absorption spectrum under UV-C light.
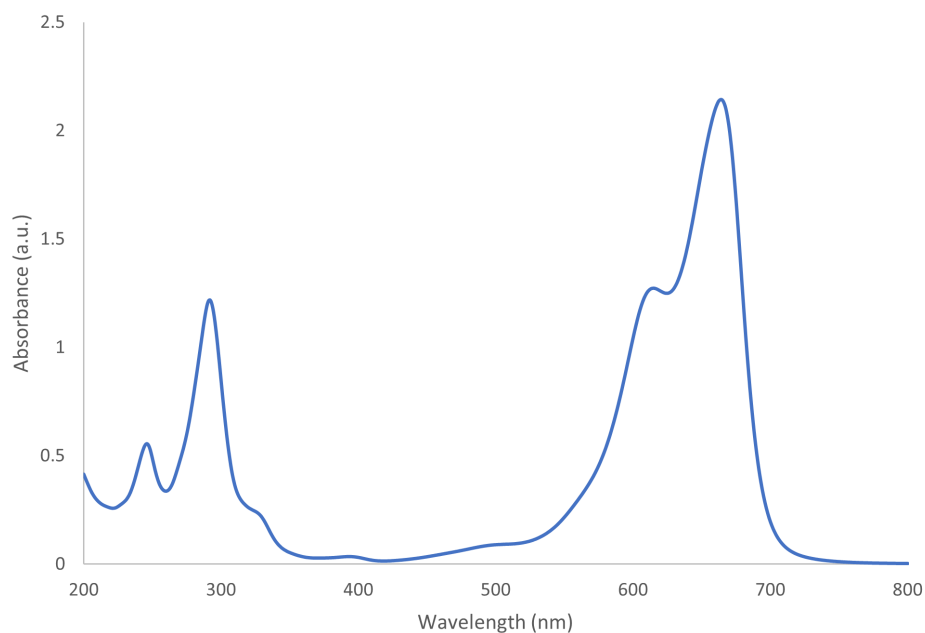
(b) MB absorption spectrum under UV-Vis light.

Figure 3.17: MB absorbance spectra.

Photodegradation Protocol

In order to define a protocol, several powder and dye concentrations were tested following protocols found in literature. The elected powder to define the protocol was TiO_2 P25.

In a 1 L flask a solution of MB was prepared and agitated magnetically for 1 h using aluminium foil as a light shield. In a 250 mL Erlenmeyer, each pigment and 250 mL of MB solution were added and the flask was covered in aluminium foil to prevent an uncontrolled photocatalytic reaction due to unwanted

exposure to ambient light. The mixture was then sonicated for 15 min and magnetically stirred at 2000 rpm for 1 h in the dark to assure the adsorption-desorption equilibrium. Past that hour, a sample was withdrawn, and the absorbance was measured to evaluate the MB absorbance by the catalyst. After that, the light was turned on and a sample was withdrawn every 20 min. The absorbance was measured using a spectrophotometer and the temperature was measured. The experiment was carried out until the MB degradation reached around 98% or after 2 h have passed. To withdraw a sample a syringe and a filter was used. The filter aims to prevent the dispersed powder to interfere with the MB solution absorbance measurement. A filter protocol had to be defined to optimize its use. Beforehand, the necessary volume to soak the filter was established. With a plunger and a syringe around 2 mL were withdrawn and passed by the filter. The filtrates absorbance was measured three times and it was confirmed that the filter was saturated after the second passage (absorbance profiles matched). Thus, the first sample withdrawn for zero time should be 4 mL to guarantee that the filter was soaked in the solution, being the following samples 2 mL. The filter being saturated means that all the porous are blocked by the powder particles. This way, only the solution, DW and MB, passes the filter. Because it revealed not to interfere to a great extend with the absorbance measurements, a single filter was used per experiment. This way, the slurry would easily reach the equilibrium again every time a sample was withdrawn. Figure **??** is an example of a set of acquired spectra.

To start, a mixture of TiO_2 P25 (400 mg/L) and MB (20 mg/L) was prepared in the darkness - sonicated for 5 min and stirred magnetically for 1h30min. Using a syringe and a filter a sample of 6 mL was withdrawn and then the absorbance was measured on a spectrophotometer. The same experiment was performed for 10 mg/L of MB to evaluate the behaviour of lower MB concentrations MB. The concentration of the sample was also studied for 400 mg/L, 500 mg/L, and 600 mg/L. After assessing the best conditions, discussed in Section 3.3.4, the next protocol was followed.
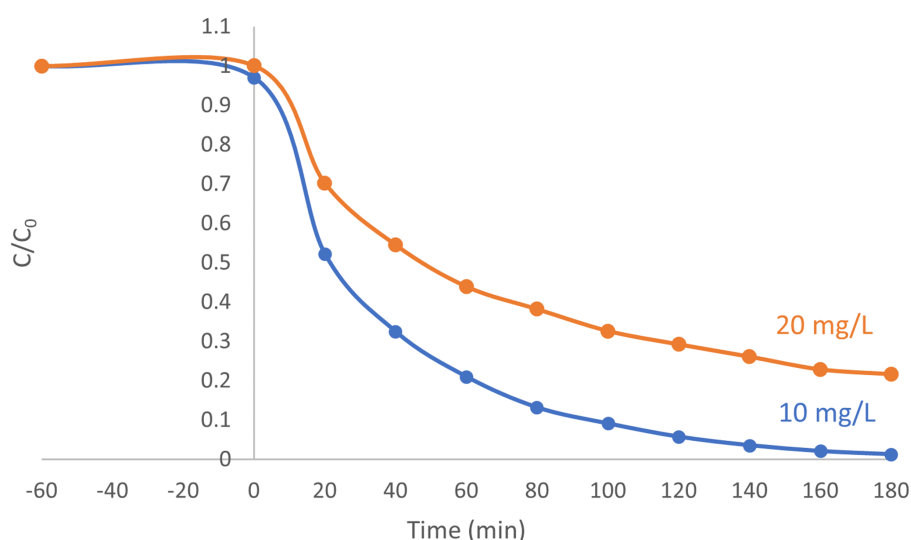

Figure 3.18: TiO_2 P25 400 mg/L with 10 mg/L and 20 mg/L. Degradation under UV light.

Being the degradation for 10 mg/L faster that for the 20 mg/L, as expected [67], the first concentration was chosen. The influence of powder's concentration was evaluated for 400 mg/L, 500 mg/L, and 600 mg/L of P25.
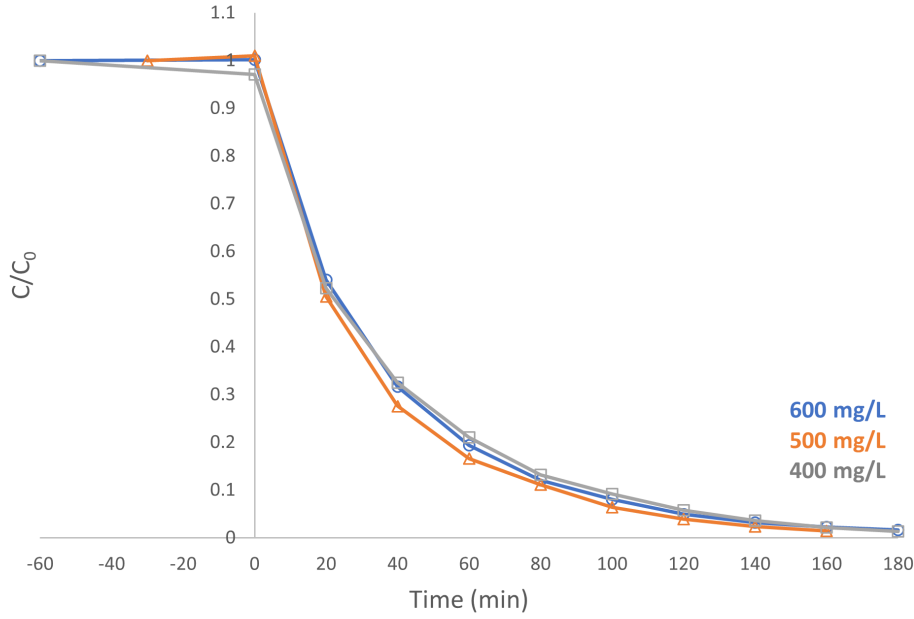
Figure 3.19: MB 10 mg/L with TiO$_2$ P25 400 mg/L, 500 mg/L, and 600 mg/L. Degradation under UV light.

In Figure 3.19 the degradation curves for each concentration present the same behaviour. The higher the concentration, the higher the number of available catalytic sites to catalyze the degradation of MB (positive effect). With this said, it was expected that the higher the concentration, the fastest the degradation process, like reported elsewhere [67]. However, that was not sustained by the experiment results, which may be explained by the possibility of light shielding by the powder itself (negative effect).

Settled the protocol, the photocatalytic experiments proceeded for every photocatalytic material. The MB degradation behaviour by each powder was then obtained by plotting all the absorbance values for 664 nm - the wavelength for which the MB light absorbance is higher.

3.3.5 Photodegradation Tests

After settling the photodegradation protocol, the results were treated in a way they could be analysed and compared. To do so, the kinetic models were obtained.

Kinetic Model

The behavior of the samples under the effect of light was described by a kinetic model. Heterogeneous photocatalysis follows a Langmuir-Hinshelwood model, which may be written as 3.7.

$$\frac{1}{r} = \frac{1}{k_r k_a C} \tag{3.6}$$

r is the reaction rate for the oxidation of reactant, k_r is the specific reaction rate constant for the oxidation of the reactant (mg/Lmin), k_a is the equilibrium constant of the reactant (L/mg) and C is the dye concentration. When C_0 is small (milimolar) the equation can be simplified to as apparent first-order equation [68].

$$C = C_0 exp(-k_{app} t) \tag{3.7}$$

To analyse the data, a normalized form of Langmuir-Hinshelwood, should be plotted in order to describe the solid-liquid reaction 4.1 [69].

27

$$ln\frac{C}{C_0} = -kt \qquad (3.8)$$

$$ln\frac{C}{C_0} = -kt \qquad (3.8)$$

Chapter 4

Results and Discussion

4.1 Characterization

As earlier mentioned, the samples in study were characterized using techniques which gave out information about their physico-chemical, structural, and optical properties - XRD and DRS techniques. As aforementioned, two of the characterization techniques, namely N_2-sorption and DLS, will not be covered here due to the inconclusive results obtained.

4.1.1 Structure Analysis

Resorting to the profile fitting based software TOPAS, and to COD and PDF databases, the quantitative phase analysis, microstructure analysis and crystal structure analysis information was obtained. To mention that the method behind the fitting based software TOPAS is the Rietveld method - technique described elsewhere [70]. By fitting a calculated profile to experimental data the present structures in the samples could be confirmed. All the information is summarized in Table 4.1. The information about crystallite size refers only to the domaining phase in the structure. All the experimental diffractograms and respective matching theoretical diffractograms may be consulted in Appendix A.

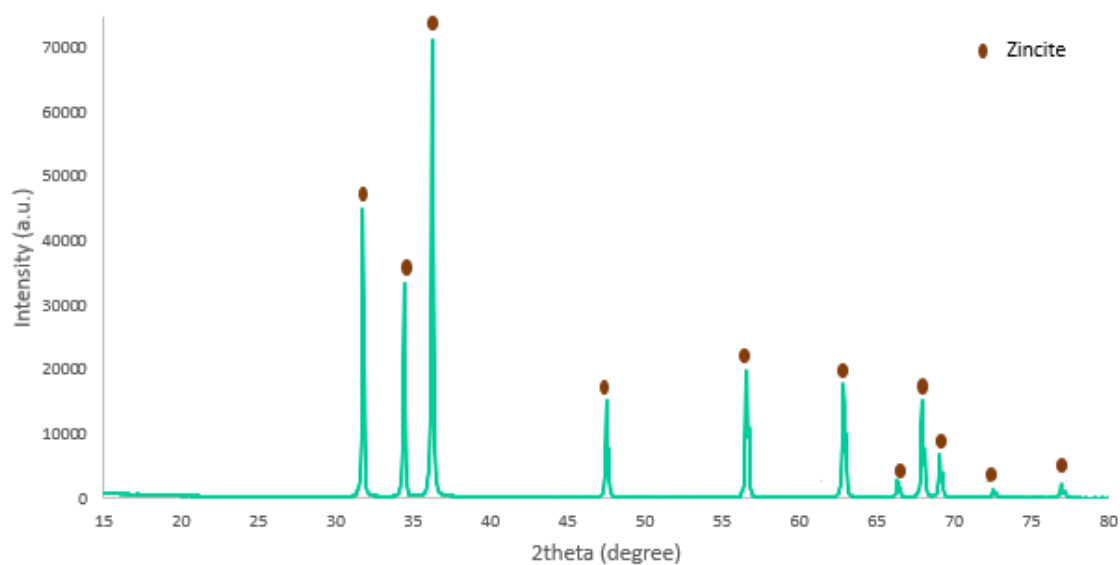Figure 4.1: Example of a one phase sample diffractogram (ZnO) - zincite COD 9004180.
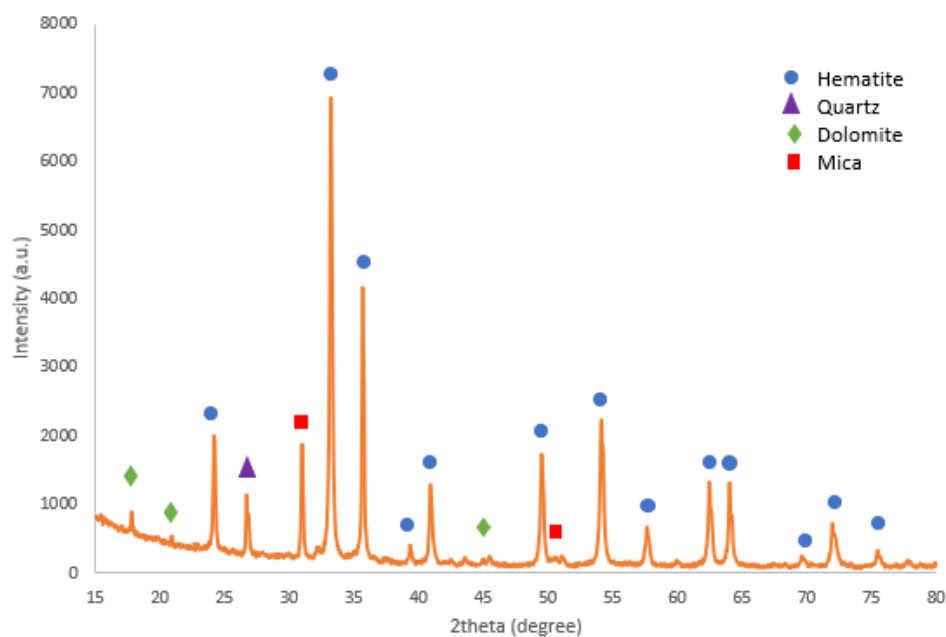

Figure 4.2: Example of a mixed-phase sample diffractogram (Fe$_2$O$_3$ lamellar) - hematite, dolomite, quartz, and mica - COD 9015964, COD 2105963, PDF 46-1045, and PDF 07-0042, respectively.

Table 4.1 summarizes all the information given by the XRD technique, information given by the supplier, and the database code of each sample's phase.

Table 4.1: XRD analysis experimental data. Mean particle size available on the supplier's data sheets. *NI* means no information.

Sample	Phase	Weight (%)	Crystallite Size (nm)	Mean Particle Size (nm)	Data base code
TiO₂ P25	Anatase	87/13	21/33	21	COD 9007531
	Rutile				COD 9007531
TiO₂ rutile	Anatase	1/99	126	290	COD 9007531
	Rutile				COD 9007531
TiO₂ anatase	Anatase	98.2/1.8	105	NI	COD 9007531
	Rutile				COD 9007531
ZnO	Zincite	100	125	NI	COD 9004180
Fe₂O₃ lamellar	Hematite/Dolomite Quartz/Mica	91/2/2/5	53	NI	COD 9015964, COD 2105963, PDF 46-1045, PDF 07-0042
Fe₂O₃ spherical	Hematite	100	50	NI	COD 9015964
FeOOH	Goethite	100	54	50 - 300	COD 1008768
Cu₂O	Cuprite	100	33	NI	COD 9007497

After examining the obtained results from the X-Ray Diffraction analysis it became clear that samples could be split into two groups: the pure ones (having mainly one phase) and the mixed-phase ones (having two or more different phases). ZnO, Fe_2O_3 spherical, FeOOH, and Cu_2O samples present only one phase. On the other hand, TiO_2 P25, TiO_2 rutile, TiO_2 anatase, and Fe_2O_3 lamellar are mix-phased. The Fe_2O_3 lamellar have four different phases, namely hematite, dolomite, quartz, and mica. Although hematite accounting for about 91 wt.%. The commercialized TiO_2 P25 (Sigma-Aldrich) diffraction peaks corresponded to reference line patterns - anatase (87 wt.%) and rutile (13 wt.%) - which confirmed the crystalline structure of TiO_2 P25. These findings are in agreement with the information provided by the supplier and with the structural analysis reported in the literature [71]. Also, TiO_2 rutile has a second phase, anatase, although representing only around 0,7% of the global weight. The same happens for TiO_2 anatase, where the rutile phase only accounts for 1.8% of the total weight.

Quartz and mica are not used as a photocatalyst, but to improve coatings characteristics such as durability. Quartz is used as sand to improve the appearance and durability of architectural and industrial paint and coatings [72]. It is usually indicated for external applications. Once dried in-depth, the coating resists chemical and atmospheric agents [73]. Mica is used as a pigment extender in coatings formulation to improve its properties, such as durability, cost, and resistance to corrosion or wear. It is used as a pigment extender that also facilitates suspension, reduces chalking, prevents shrinking and shearing of the paint film increases the resistance of the paint film to water penetration and weathering and brightens the tone of coloured pigments. Mica also promotes paint adhesion in aqueous and oleoresinous formulations. On the other hand, dolomite, a low-cost natural mineral, exhibits properties of semiconductor photocatalyst in photoreactions. However, due to its wide band gap value, 5,02 eV, may have not contributed to better photocatalytic performance, but only as a filler on the coatings formulation, since it is an inexpensive mineral that may provide opaqueness to paint films [72].

The TiO_2-based photocatalytic main phases, anatase and rutile, are acknowledged photocatalyic active structures [47]. On the other hand, non-TiO_2 - photocatalyst main phases - hematite, goethite, cuprite, zincite - are still in study. Studies which defend its photocatalytic activity [51, 74–76]. This belief supported by several articles encouraged the determination of their potential as photocatalysts.

Regarding crystallite size, TiO_2 rutile, TiO_2 anatase, and ZnO have a crystallite size superior to 100 nm, may being considered a microstructure. Among white pigments, TiO_2 P25 is the only with a nanostructure (21/33 nm). Fe-based have around the same crystallite size (50 nm), while Cu_2O has a smaller size, 33 nm. Worth mentioning that the state-of-the-art TiO_2 P25 also matched the anatase:rutile ratio [47].

When comparing crystallite size and mean particle size, one may evaluate if the particles are poly-crystalline or single-crystal. Looking at the given information by the supplier, one can say that TiO_2 P25 matches for crystallite size and mean particle size. On the contrary, that does not happen with TiO_2 rutile, TiO_2 anatase, and FeOOH, so they are polycrystalline.

4.1.2 Optical Properties

Optical and electronic properties were studied resorting to UV-Vis DRS technique. The light absorbance, as well as the band gap value determined from Tauc plot analysis, will be discussed here.

Absorbance

Each sample was subjected to the DRS technique in the powder form. From that experiment, reflectance plots were obtained and converted to Kubelka-Munk functions, Equation 3.2.

The following set of spectra, Figures 4.3 and 4.4, present the information obtained by the spectropho-tometer, which will be grouped as white and color pigments due to their behaviour.
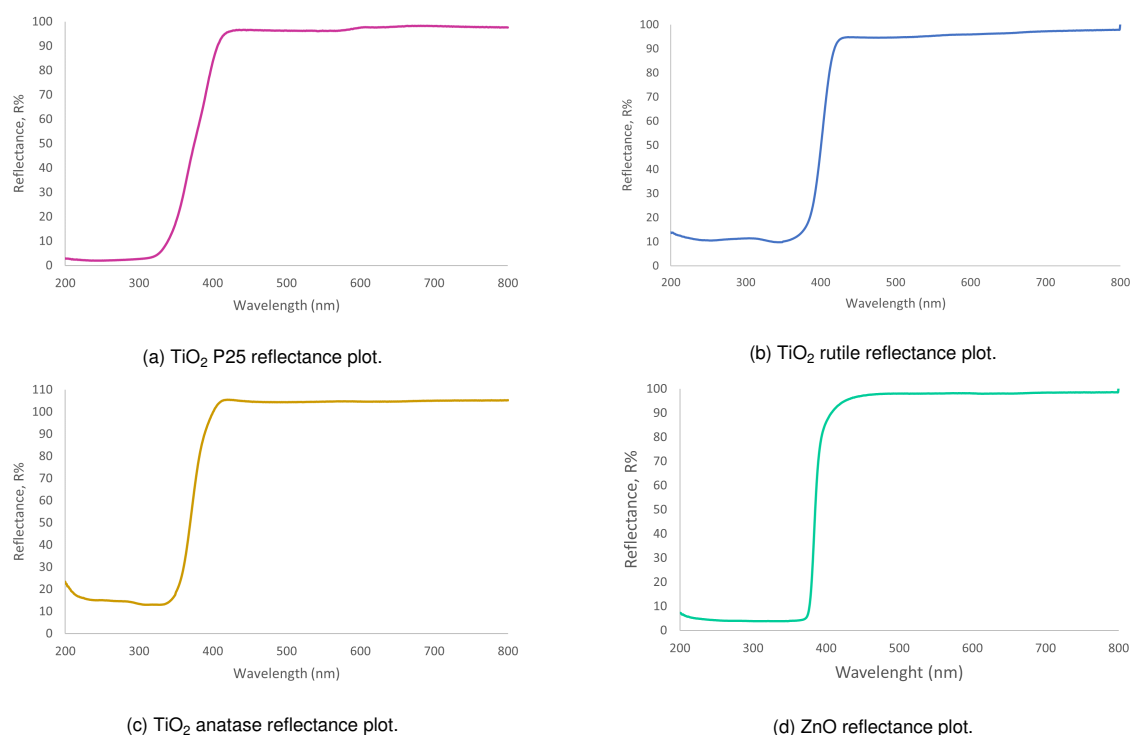

(a) TiO_2 P25 reflectance plot.

(b) TiO_2 rutile reflectance plot.

(c) TiO_2 anatase reflectance plot.

(d) ZnO reflectance plot.

Figure 4.3: Reflectance plots of the white pigments.

(a) Fe$_2$O$_3$ lamellar reflectance plot.

(b) Fe$_2$O$_3$ spherical reflectance plot.
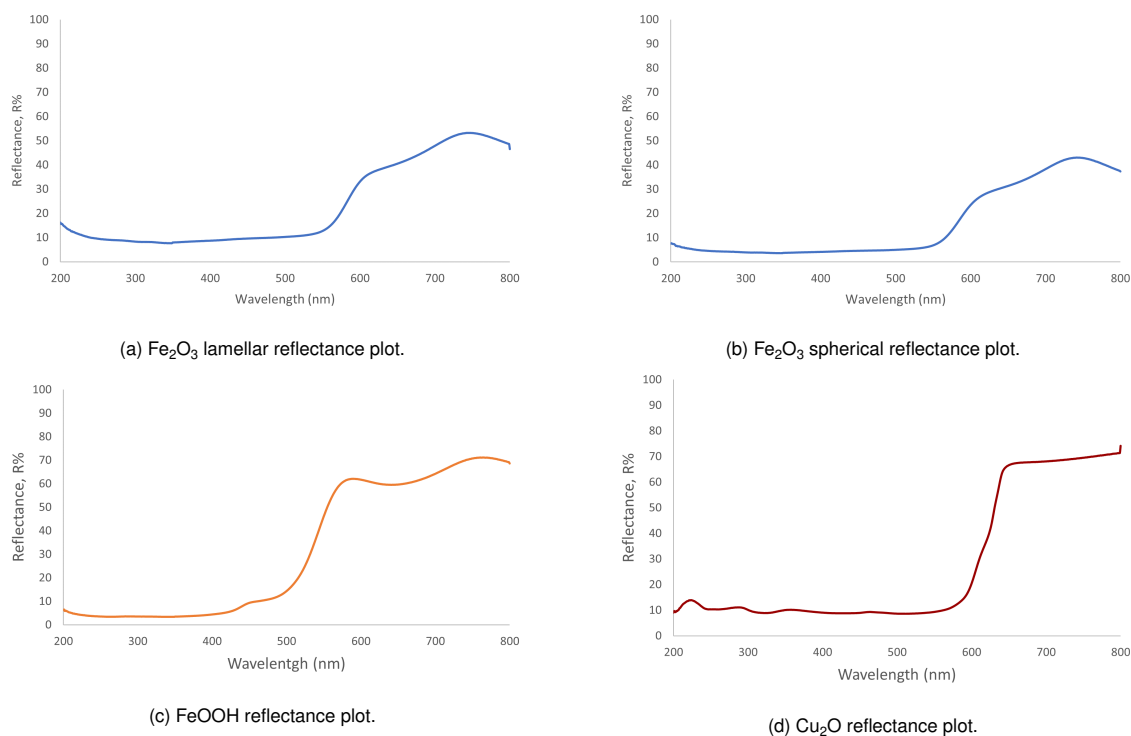
(c) FeOOH reflectance plot.

(d) Cu$_2$O reflectance plot.

Figure 4.4: Reflectance plots of the color pigments.

TiO$_2$-based photocatalysts and ZnO present the same absorption threshold. All four absorb light under the 400 nm (UV band). All the radiation higher than 400 nm is reflected. Regarding Fe$_2$O$_3$ spherical and lamellar they both absorb radiation below 600 nm. FeOOH absorbs for lower wavelengths than 500 nm. Cu$_2$O absorbs for lower values than 600 nm. All the Fe-based samples and Cu$_2$O absorb part of the light in the UV-Vis region - check Figure 3.13. This behavior in the UV-Vis region proved them to be potential photocatalysts.

Band Gap

The band gap value, of paramount importance to predict and to comment on the photocatalytic activity, was obtained resorting to the DRS technique and the Kubelka- Munk equation, Equation 3.3, as explained in Section 3.2.2.

Both direct and indirect electronic transitions, check Table 3.2, were plotted and the band gap was obtained. To assess which transition is believed to be each pigment's type of transition, an extensive review on that matter should be done. Direct and indirect transition fittings will be both presented and discussed, once the band gap values have been indistinctively obtained in the literature.

Since the main goal of this project is the comparison between potential candidates to find alternatives to TiO$_2$-based photocatalysts, a systematic protocol for achieving reproducible and meaningful results is a priority from the benchmarking point of view. The adopted method to find the *Eg* value consists in making linear regressions. Although quite sensible to interpretation, this empirical way of obtaining the *Eg* value is acknowledged and very much used by the scientific community. Depending on the spectrum profile, one or two tangent lines are drawn, assuming in this last case the intersection to be the *Eg* value [62]. Those lines were drawn tangent to the far left curve, on the first method, or tangent to the two far-left curves on the plot, on the second method. The absorbance at energies below the *Eg* of occurs in the case of a defect, doped, bulk or surface modified materials [62].

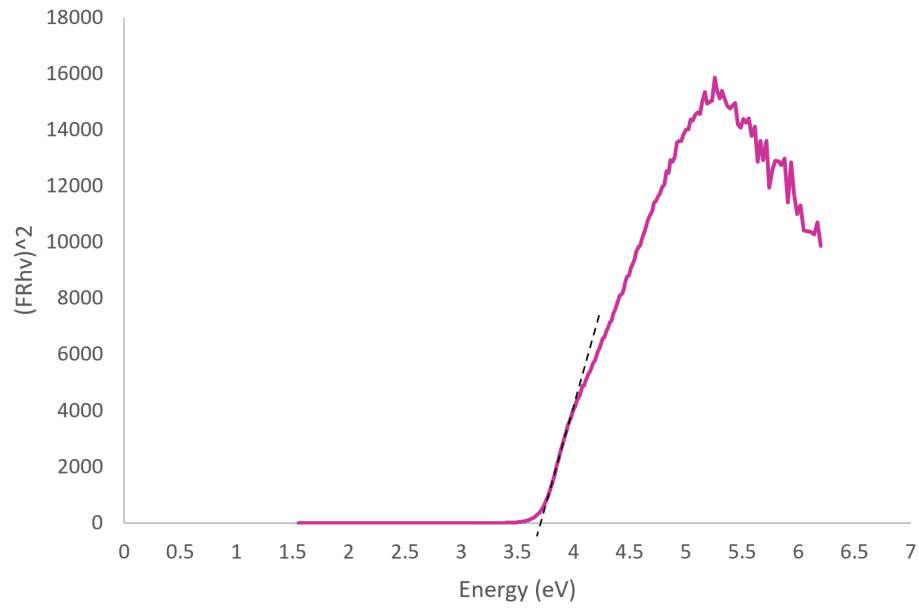In the following Figure 4.5 and 4.6 both TiO$_2$ P25 Tauc plot were done for direct and indirect transition.

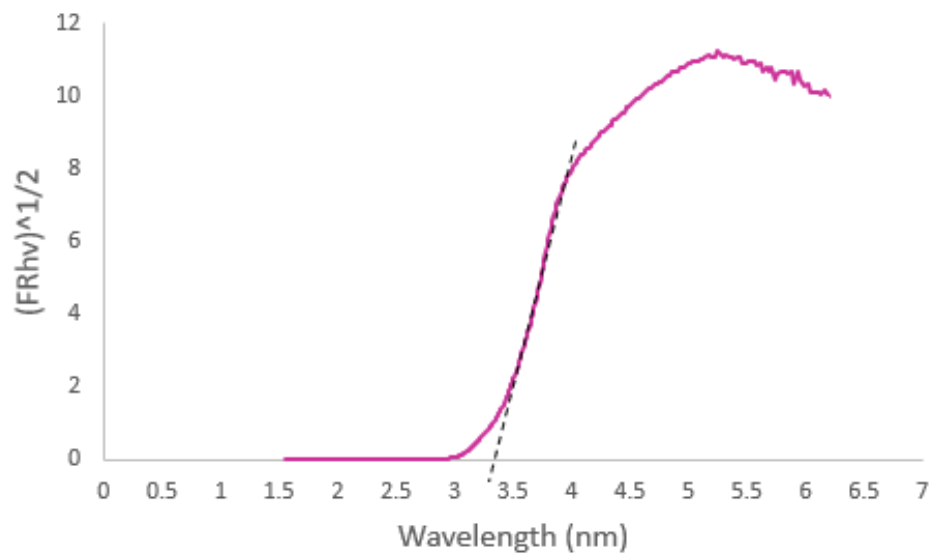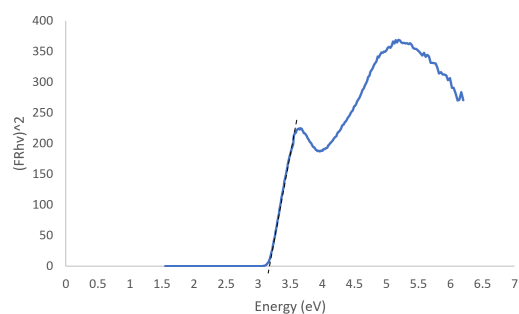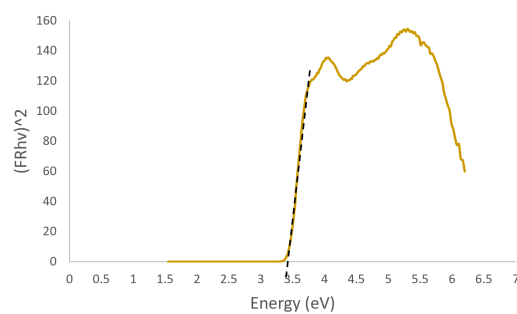Figure 4.5: TiO$_2$ P25 direct transition.

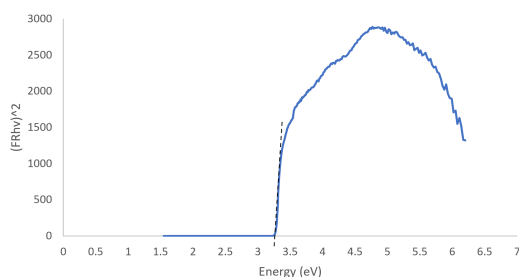
Figure 4.6: TiO$_2$ P25 indirect transition.

In the following Tauc plots the direct transitions - Figures 4.7 and 4.8 were plotted for the rest of the samples. The indirect Tauc plots may be consulted in Appendix B.
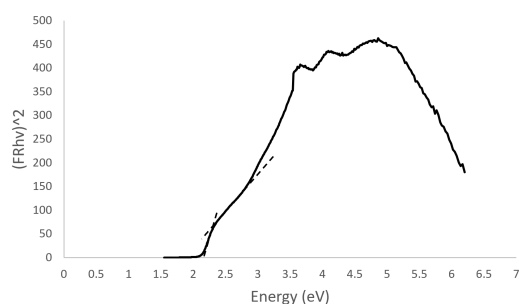
(a) TiO$_2$ rutile direct transition.

(b) TiO$_2$ anatase direct transition.

(c) ZnO direct transition.

Figure 4.7: Tauc plots - direct transitions of the white pigments.

(a) Fe$_2$O$_3$ lamellar direct transition.
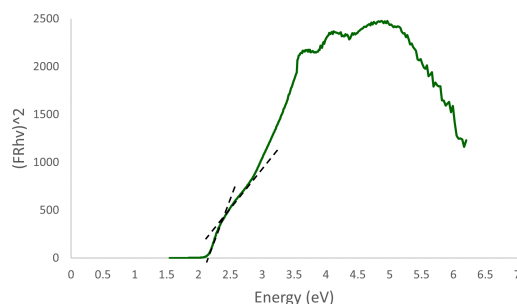
(b) Fe$_2$O$_3$ spherical direct transition.
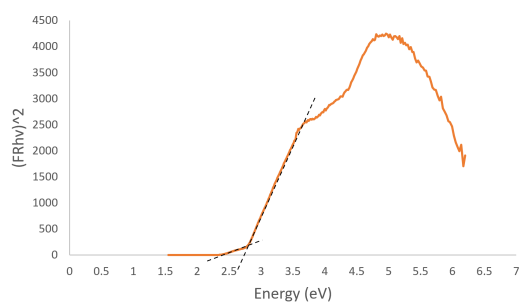
(c) FeOOH direct transition.
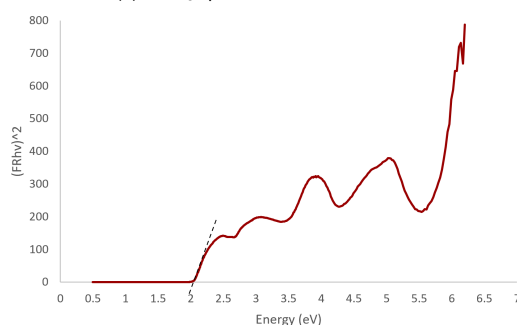
(d) Cu$_2$O direct transition.

Figure 4.8: Tauc plots - direct transitions of color pigments.

An interval of values was chosen and the characteristics of the tangent line were obtained. The reliability of the resultant tangent line may be conferred by consulting the statistical information, namely the R^2. The *Eg* value is computed by dividing the *Intercept* by the *X Variable*. For the two tangent lines approach, the intersection of this two lines gave out the *Eg* value - Appendix C.

In tables 4.2 and 4.3 the band gap value obtained, as well as the band gap literature value and the type of electronic transition may be consulted - [77–82].

35

Table 4.2: Experimental electronic characteristics of the samples and the value found in the literature. One tangent line approach.

Sample	Band Gap Direct	Band Gap Indirect	Band Gap Literature
TiO$_2$ P25	3.7	3.3	3.20
TiO$_2$ rutile	3.2	3.2	3.00
TiO$_2$ anatase	3.4	3.2	3.20
ZnO	3.3	3.2	3.25

Table 4.3: Experimental electronic characteristics of the samples and the values found in the literature. Obtained band gap using the tangent lines intersection method.

Sample	Band Gap Direct	Band Gap Indirect	Band Gap Literature
Fe$_2$O$_3$ lamellar	2.3	2.4	1.97
Fe$_2$O$_3$ spherical	2.3	2.4	1.97
FeOOH	2.7	2.7	2.15
Cu$_2$O	2.0	2.0	2.35

Looking at Table 4.2 and Table 4.3 it may be said that the experimental value is in accordance with the one reported in the literature for white pigments - Table 4.2. In the case of colour samples, the difference is noticeable - Table 4.3. The possibility of more transitions favoured by the interaction with the visible radiation can explain the so complex profile of the colour pigments. That behaviour contributes to a less consensual approach of this practical method once it depends entirely on the operator's judgement. This can make the confrontation of experimental data with the literature challenging, which urges the need to adopt a systematic and straightforward approach so results may be compared and conclusions are drawn more easily.

4.2 Photocatalytic Performance Evaluation

After the pre-photodegradation tests, and before starting the photodegradation tests, some main conclusions were drawn. No photolysis was registered for the two type of lights, the equilibrium adsorption-desorption was reached, and the dispersibility test in DW revealed Cu$_2$O hidrophobicity. Bearing these findings in mind, the photocatalytic performance evaluation proceeded.

The photocatalytic activity of all the samples was evaluated by measuring the photocatalytic decomposition of MB under UV-C and UV-Vis illumination. The MB degradation behaviour of all the samples is represented in Figure 4.9 and 4.10.
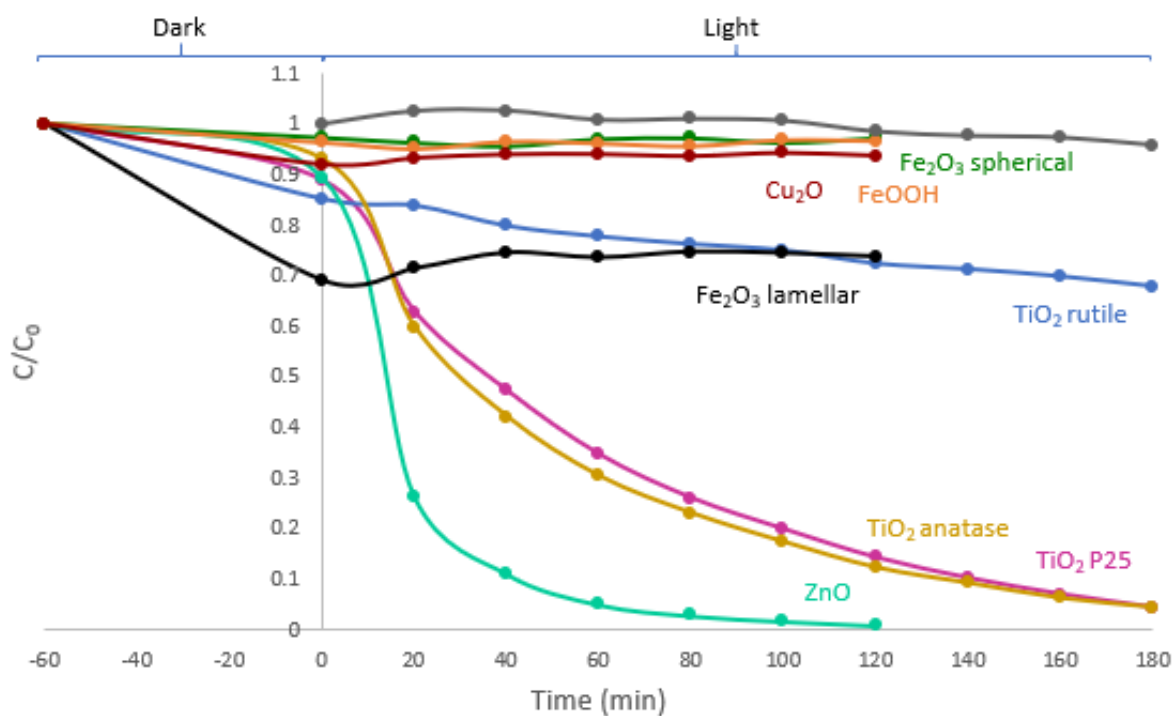
Figure 4.9: MB (10 mg/L) degradation by the catalyst (400 mg/L) under UV-C light.
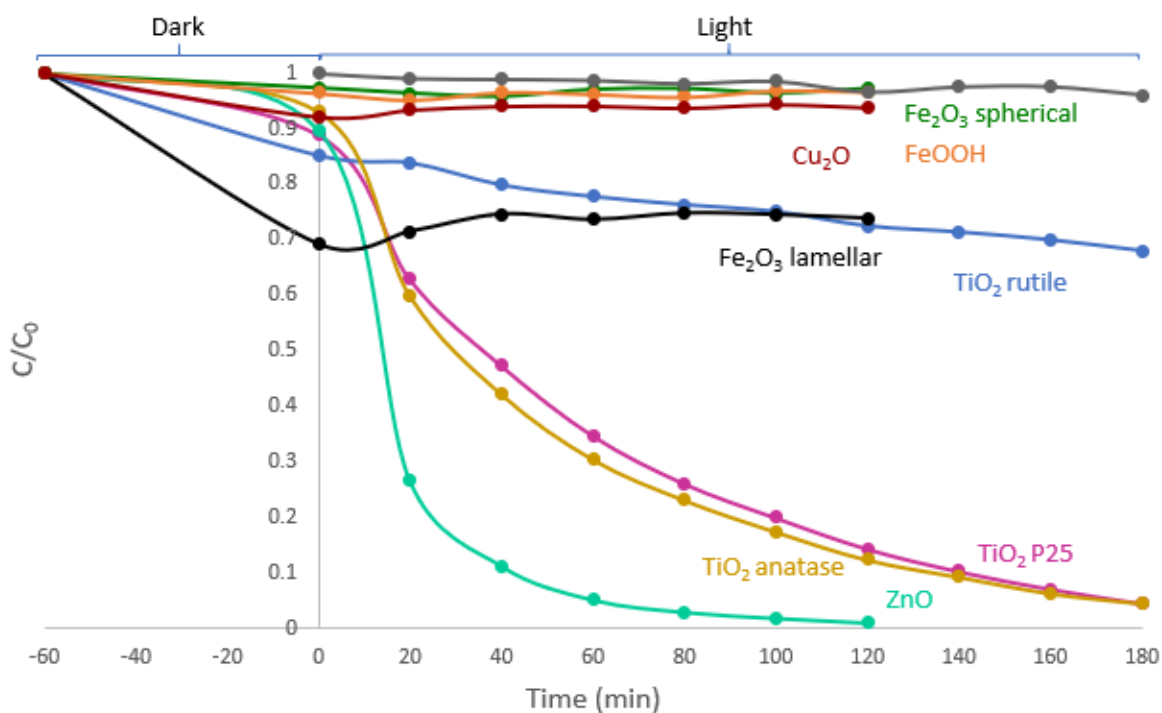
Figure 4.10: MB (10 mg/L) degradation by the catalyst (400 mg/L) under UV-Vis light.

In the Dark, it is believed not to occur MB degradation. The decrease of C/C_0 in the dark, spotted in Figures 4.9 and 4.10, may be explained by the adsorption of the dye by the photocatalyst phenomenon, once no degradation is excepted. The Fe_2O_3 lamellar is the sample that adsorbs the most. That may be due to its lamellar structure, which may trap more MB molecules. To check this assumption, further calculations should be performed. Also, further experiments could be performed to sustain this premise,

37

such as building the profile of MB adsorption by the Fe_2O_3 lamellar and also studying the textural properties of the powder (i.e N_2-adsorption).

UV-C light

Under UV-C illumination, different degradation behaviours have been registered. TiO_2 P25, TiO_2 rutile, TiO_2 anatase, and ZnO are the pigments with the best MB degradation performance. ZnO showed a MB degradation of around 100% after 2 h while TiO_2 P25, and TiO_2 anatase degraded more than 90% after 3 h. TiO_2 rutile went no further than 20% after 3 h. Fe-based and Cu_2O samples revealed the lowest activity under light exposure holding around 0% MB degradation after 3 h.

UV-Vis light

Under UV-Vis illumination, the degradation behaviour registered revealed an identical behaviour to the UV-C light. TiO_2 P25, TiO_2 rutile, TiO_2 anatase, and ZnO were again the pigments with the best MB degradation performance. ZnO showed a MB degradation of around 100% after 2 h while TiO_2 P25, and TiO_2 anatase degraded more than 90% after 3 h. TiO_2 rutile went no further than 20% after 3 h. Fe-based and Cu_2O samples revealed the lowest activity under light exposure holding around 0% MB degradation after 3 h.

Kinetic model

A normalized form of Langmuir-Hinshelwood, was plotted in order to describe the solid-liquid reaction 4.1 [69].

$$ln\frac{C}{C_0} = -kt \tag{4.1}$$

Figures 4.12 and 4.11 represent the kinetic model of the MB degradation under UV-C and UV-Vis following that model.
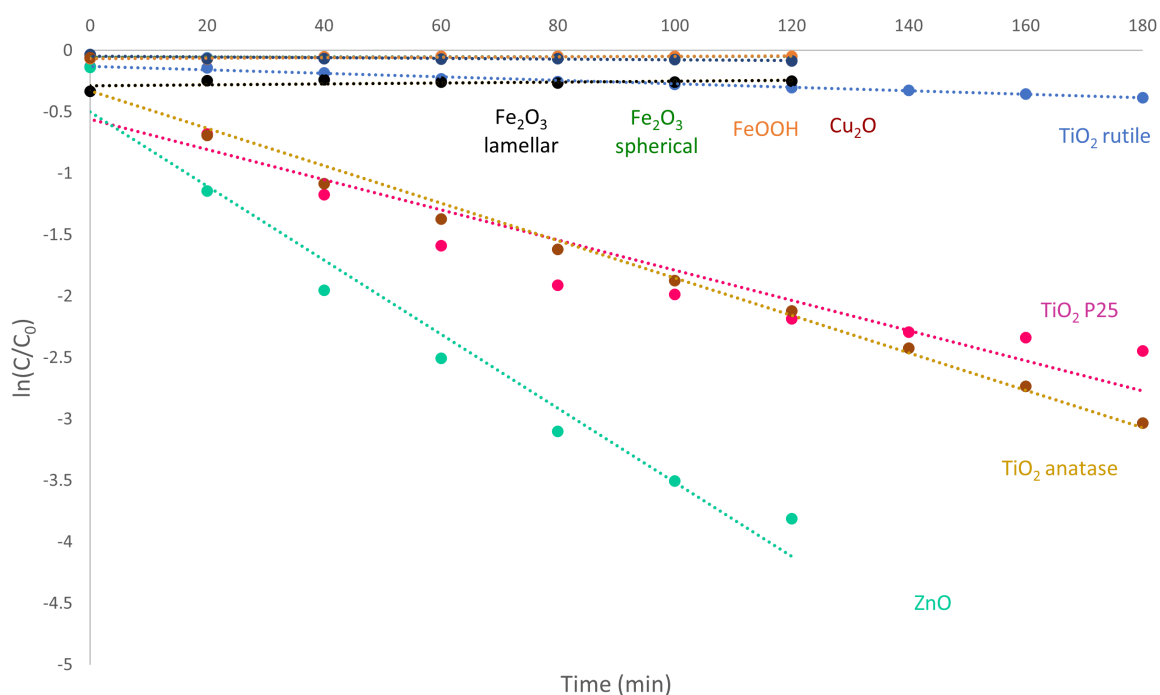

Figure 4.11: Kinetic model: MB (10 mg/L) degradation by the catalysts (400 mg/L) under UV-C.
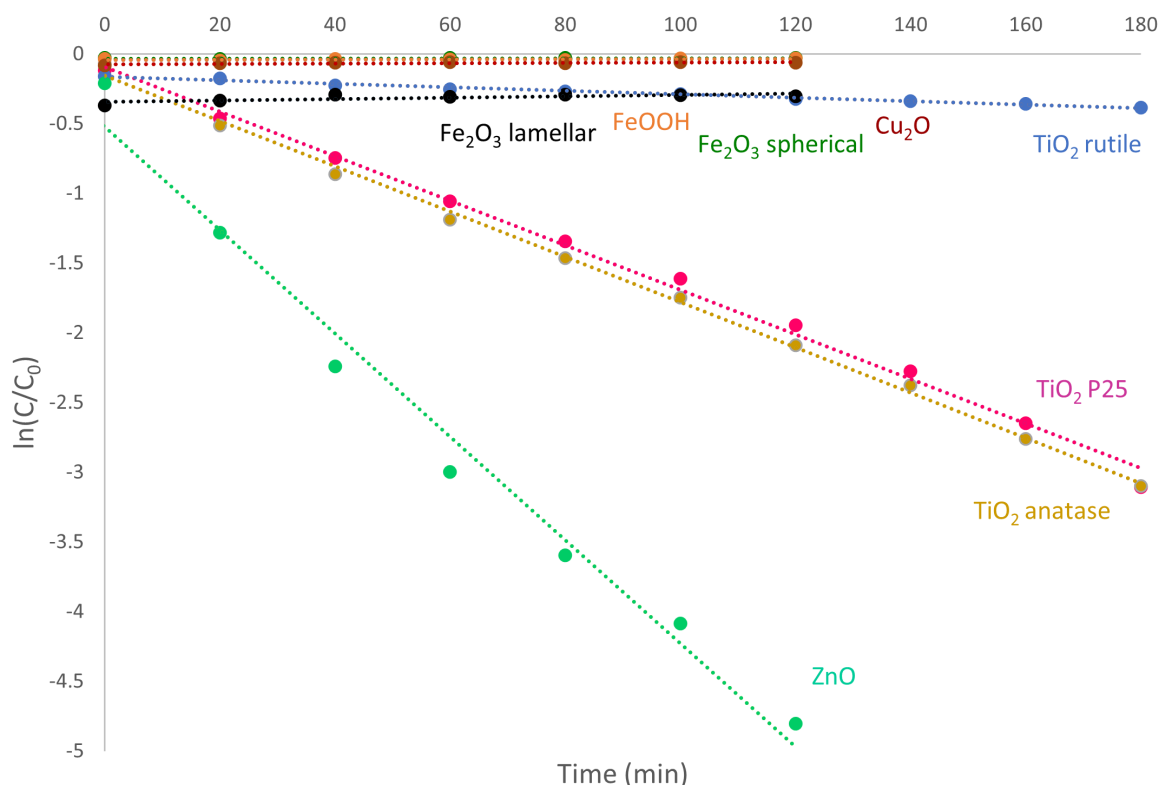
38

Figure 4.12: Kinetic model: MB (10 mg/L) degradation by the catalysts (400 mg/L) under UV-Vis.

The reaction rate constant values, for both light sources and runs, are in Table 4.4. The Fe-based samples, as well as Cu_2O, are not represented here because the regression did not provide realistic rate constants, ranging from (0.002 to 0.05)x10^{-2} min^{-1} in absolute value.

Table 4.4: Reaction rate constant, k, for each light source (UV-C and UV-Vis) and for both runs.

Powder	kx10^{-2} (min^{-1}) UV-C	kx10^{-2} (min^{-1}) UV-Vis
TiO$_2$ P25	1.20 / 2.30	1.30 / 1.60
TiO$_2$ rutile	0.14 / 0.16	0.13 / 0.17
TiO$_2$ anatase	1.50 / 1.70	1.40 / 1.60
ZnO	3.00 / 3.50	3.60 / 3.70

All the pigments confirmed the pseudo first-order kinetics fitting ($0.8758 < R^2 < 0.9886$).

UV-C light

In Figure 4.11, TiO$_2$ P25, TiO$_2$ anatase, and ZnO are the samples which showed the best performance - TiO$_2$ P25 (1.20x10^{-2} min^{-1}) < TiO$_2$ anatase (1.50x10^{-2} min^{-1}) < ZnO (3.00x10^{-2} min^{-1}). TiO$_2$ rutile, among the best performances, is the one with the lowest reaction rate constant - 0.14x10^{-2} min^{-1}. As said previously, Fe-based and Cu$_2$O did not provide realistic constants.

UV-Vis light

In Figure 4.12, TiO$_2$ P25, TiO$_2$ anatase, and ZnO are the samples which showed the best performance - TiO$_2$ P25 (1.30x10^{-2} min^{-1}) < TiO$_2$ anatase (1.40x10^{-2} min^{-1}) < ZnO (3.60x10^{-2} min^{-1}). TiO$_2$ rutile, among the best performances detained by the white powders, is the one with the lowest reaction rate constant - 0.13x10^{-2} min^{-1}. As said previously, Fe-based and Cu$_2$O did not provide realistic constants.

Table 4.5: Summary of the main characteristics of each sample.

Sample	Band Gap Direct	Band Gap Indirect	$kx10^{-2}$ (min^{-1}) UV-C	$kx10^{-2}$ (min^{-1}) UV-Vis
TiO_2 P25	3.3	3.7	1.20/2.30	1.30/1.60
TiO_2 Rutile	3.2	3.4	0.14/0.16	0.13/0.17
TiO_2 Anatase	3.2	3.2	1.50/1.70	1.40/1.60
ZnO	3.2	3.3	3.00/3.50	3.60/3.70
Fe_2O_3 lamellar	2.4	2.3	$\sim$0	$\sim$0
Fe_2O_3 spherical	2.4	2.3	$\sim$0	$\sim$0
FeOOH	2.7	2.7	$\sim$0	$\sim$0
Cu_2O	2.0	2.0	$\sim$0	$\sim$0

The difference between performances may be explained by several factors, such as band gap value, VB/CB position, crystallite size, particle morphology, and phase activity. However, only the band gap, crystallite phase, and crystallite size will be discussed based on the XRD and DRS results.

Regarding what was stated in Section 4.1.2, samples may be divided into two groups concerning their light absorption behaviour - white and colour pigments. The band gap value may give an idea of how good a sample is under a certain type of light source. Narrower band gaps (colour samples) need less energetic light to form a pair electron/hole. On the contrary, wider band gaps (white pigments) need more energy for a pair electron/hole to occur. The band gap width was obtained to comply with the absorbance region of the samples covered before. Meaning, wider band gap semiconductors have an electron/hole pair with more potential energy than the pairs formed in narrower band gaps.

Wider band gaps present a major drawback. Once UV light accounts for only around 8% of the spectrum of light, that makes them less active under sunlight. Also, indoor environments will not favour this kind of photocatalysts where common light has almost no UV component. Narrower band gap semiconductors will need less energetic light to form an electron/hole pair (UV-Vis). In short, wider band gap semiconductors will have their applications shortened under sunlight and indoor light.

In short, colour pigments showed a low activity under both types of lights, while white pigments showed better performance under UV-C and UV-Vis - as k values suggest (Table 4.4). However, there is another aspect that should be taken into consideration when evaluating pigments performance - the VB/CB position, Figure 4.13.
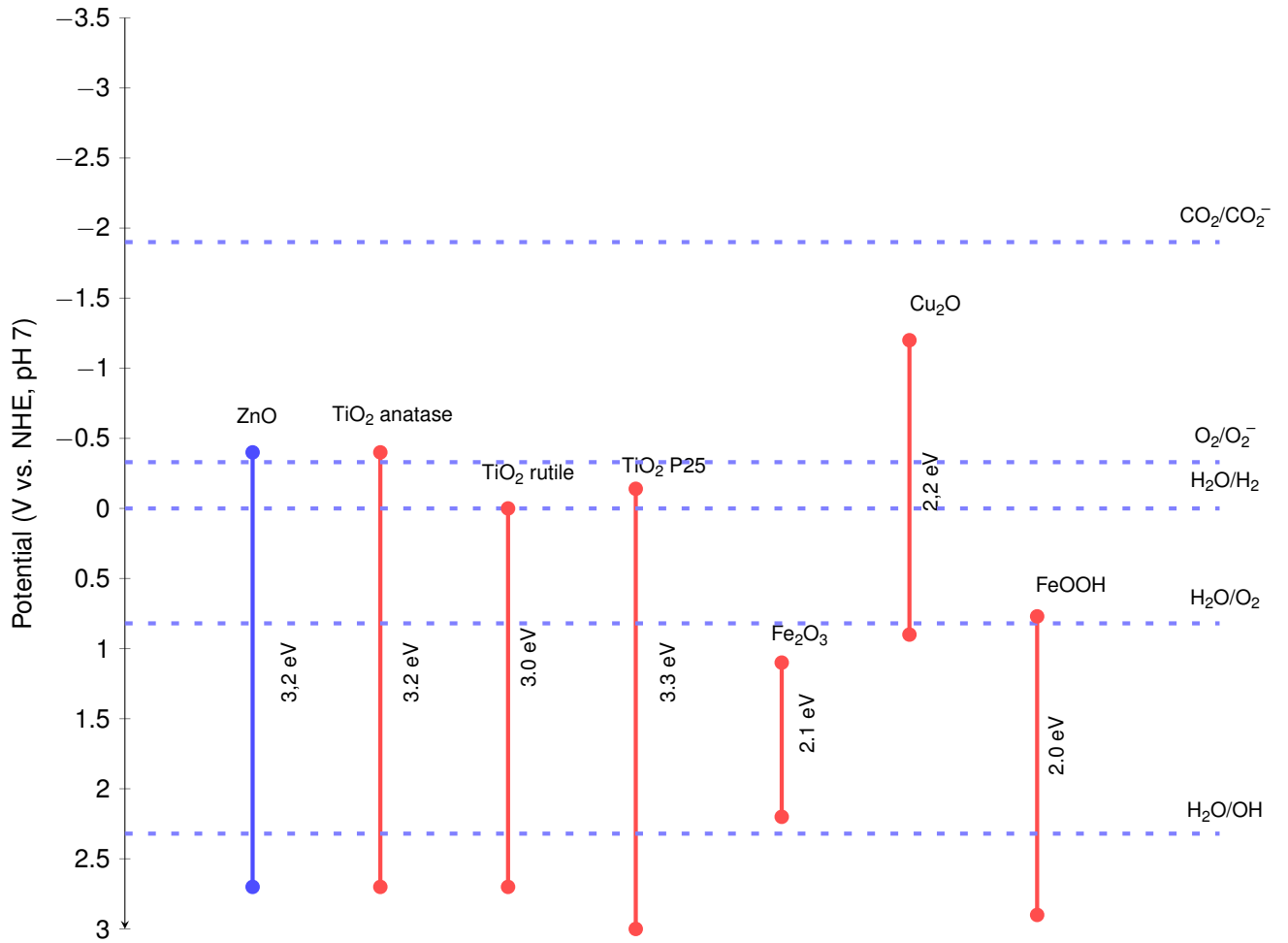
Figure 4.13: Valence and conduction band samples' position [9].

The band gap position may enable reduction and/or oxidation reactions depending on the positions of the VB/CB [44]. The VB hole formed when the migration of the electron to the conduction band is a strong oxidizing agent and it is capable of oxidizing electron donor molecules adsorbed on the surface. The CB electron is a powerful reducing agent and may reduce acceptor molecules [73].

The following equations happen sequentially on photocatalyic reactions. TiO_2 will be given as an example.

$$TiO_2 \rightarrow h^+ + e^- \tag{4.2}$$

$$H_2O \rightarrow H^+ + OH^- \tag{4.3}$$

$$h^+ + OH^- \rightarrow OH^\cdot \tag{4.4}$$

$$e^- + O_2 \rightarrow O_2^- \tag{4.5}$$

$$H^- + O_2^- \rightarrow HO_2^\cdot \tag{4.6}$$

Wider band gap samples, namely TiO_2 P25, TiO_2 anatase and ZnO, have their valence and conduc-

tion bands well aligned to trigger oxidation and reduction reactions. The proper alignment, along with the wide band gap, grant these samples the best photocatalytic performance. The narrower band gap samples present a lower to none activity because of the band alignment which does not allow reduction reactions to occur.

Chapter 5

Conclusions and Future Work

The main objective of this work was to select and compare a set of photocatalytic pigments already in use in the industry. A benchmarking approach put TiO_2-based photocatalysts against non-TiO_2-based alternatives. The TiO_2 photocatalytic pigment was selected because it is an acknowledged state-of-the-art pigment.

All the samples in the study were characterized using techniques that gave out information about their physicochemical, structural, and optical properties, namely XRD and UV-DRS techniques. Pigments have shown the presence of one or more phases. In the case of TiO_2 rutile, TiO_2 anatase, ZnO, Cu_2O, Fe_2O_3 spherical, and FeOOH they are all pure - having the first two minute quantities of other phases (TiO_2 rutile with 1 wt.% anatase and TiO_2 anatase with 2 wt.%). On the other hand, Fe_2O_3 lamellar, and TiO_2 P25 revealed the presence of two or more phases. The TiO_2-based photocatalysts main phases, anatase and rutile, are acknowledged photocatalytic active structures. Oppositely, non-TiO_2-photocatalyst main phases - hematite, goethite, cuprite, zincite - are still in study. Fe_2O_3 lamellar has four different phases - hematite, dolomite, quartz, and mica. Only quartz and mica are known as non-active under light exposure, while hematite and dolomite are active under light exposure. However, the presence of dolomite did not enhance the photocatalytic activity of Fe_2O_3 lamellar what may be due to its wide band gap, 5.2 eV. Regarding the crystalline size, TiO_2 rutile, TiO_2 anatase, and ZnO crystallites have more than 100 nm. The TiO_2 P25, Fe_2O_3 lamellar, Fe_2O_3 spherical, FeOOH, and Cu_2O crystallites have shown to have between 21 - 54 nm. The DRS analysis provided the band gap values which split the pigments into the same two different groups - the white pigments (around 3.0 eV) and the colour pigments (around 2.0 eV).

The photo-degradation protocol revealed pigments performances. ZnO is the only non-TiO_2-based pigment which showed a better performance than TiO_2 P25 under UV-C and UV-Vis lights. Fe_2O_3 lamellar, Fe_2O_3 spherical, FeOOH, and Cu_2O did not degrade methylene blue, while TiO_2 rutile, TiO_2 anatase, and TiO_2 P25 did degrade the dye at some extent. Not only does the band gap value dictate the efficacy of a photocatalytic pigment, but few other aspects such as the position of the valance and conduction band. ZnO band's position enables oxidation and reduction reactions to occur.

Even though ZnO proved to be a good alternative to TiO_2-based photocatalysts, further characterization must be done as well as photodegradation experiments. Regarding characterization, SEM should be carried out to corroborate XRD results and confirm the structure. N2-physisorption and DLS techniques should be performed again. The first will give out information about the textural properties of the sample, while the latter will determine the size distribution profile of the particles, corroborating, or not, the XRD results. Adopting other types of light sources, with less UV component and more Vis component, would be interesting to evaluate the performance of each sample under this less energetic light source. And lastly, elected the ZnO, the formulation of a photocatalytic coating containing this pigment

and the evaluation of its activity, including comparison with reference coatings containing TiO$_2$ NPs, should be performed.

Bibliography

[1] S B Lyon, R Bingham, and D J Mills. Advances in corrosion protection by organic coatings: What we know and what we would like to know. *Progress in Organic Coatings*, 102:2–7, 2017.

[2] Tong Zhang, Xiaoguang Wang, and Xiwang Zhang. Recent progress in TiO2-mediated solar photocatalysis for industrial wastewater treatment. *International Journal of Photoenergy*, 2014(March 2015), 2014.

[3] What is photocatalyst — ecolotex thailand.

[4] J. Epp. X-ray diffraction (XRD) techniques for materials characterization. *Materials Characterization Using Nondestructive Evaluation (NDE) Methods*, pages 81–124, jan 2016.

[5] Difratómetros de raios x — bruker.

[6] Varian Cary 4000, 5000 and 6000i Spectrophotometers.

[7] P. Sivarajah, A. A. Maznev, B. K. Ofori-Okai, and K. A. Nelson. What is the brillouin zone of an anisotropic photonic crystal? *Physical Review B*, 93:054204, 2 2016.

[8] S. T.T. Le, W. Khanitchaidecha, and A. Nakaruk. Photocatalytic reactor for organic compound removal using photocatalytic mechanism. *Bulletin of Materials Science*, 39(2):569–572, 2016.

[9] D Durgalakshmi, R Ajay Rakkesh, Saravanan Rajendran, and Mu. Naushad. Principles and Mechanisms of Green Photocatalysis. 15110019(September 2019):1–24, 2020.

[10] Organic Coatings. *Organic Coatings*.

[11] E. Luévano-Hipólito, L. M. Torres-Martínez, and L. V.F. Cantú-Castro. Self-cleaning coatings based on fly ash and bismuth-photocatalysts: Bi2O3, Bi2O2CO3, BiOI, BiVO4, BiPO4. *Construction and Building Materials*, 220:206–213, 2019.

[12] Sigrid Douven, Julien G Mahy, C Wolfs, Charles Reyserhove, Dirk Poelman, François Devred, Eric M Gaigneaux, and D Lambert. Efficient N, Fe Co-Doped TiO2 Active under Cost-Effective Visible LED Light: From Powders to Films. (x).

[13] Sustainable Development Goals - UNITED NATIONS.

[14] European Union Commission Delegated Regulation (EU). Mixtures containing titanium dioxide. 10(December 2016):1–21, 2020.

[15] Artur Goldschmidt and Hans-Joachim Streitberger. *Basics of Coating Technology*. 2007.

[16] Anallyne Nayara Carvalho Oliveira Cambrussi, Alan Ícaro Sousa Morais, Alex de Meireles Neris, Josy Anteveli Osajima, Edson Cavalcanti da Silva Filho, and Alessandra Braga Ribeiro. Photodegradation study of TiO2 and ZnO in suspension using miniaturized tests. *Matéria (Rio de Janeiro)*, 24(4), 2019.

[17] Zinc oxide - cameo.

[18] Dorian Hanaor, Charles Sorrell, Dorian A H Hanaor, and Charles C Sorrell. Review of the anatase to rutile phase transformation. *Journal of Ma-terials Science*, 46, 2011.

[19] Yi Jia Chen and Tse Shan Lin. Enhancement of visible-light photocatalytic efficiency of TiO2 nanopowder by anatase/rutile dual phase formation. *Applied Sciences (Switzerland)*, 10(18), 2020.

[20] Chin Boon Ong, Law Yong Ng, and Abdul Wahab Mohammad. A review of ZnO nanoparticles as solar photocatalysts: Synthesis, mechanisms and applications. *Renewable and Sustainable Energy Reviews*, 81(August 2017):536–551, 2018.

[21] Eva de Lucas-Gil, Javier Menéndez, Laura Pascual, José F. Fernández, and Fernando Rubio-Marcos. The benefits of the ZnO/clay composite formation as a promising antifungal coating for paint applications. *Applied Sciences (Switzerland)*, 10(4):1–11, 2020.

[22] Saeed Behzadinasab, Alex Chin, Mohsen Hosseini, Leo Poon, and William A Ducker. A Surface Coating that Rapidly Inactivates SARS-CoV-2. *ACS Applied Materials & Interfaces*, 12(31):34723–34727, 2020.

[23] Raymond H Fernando. Nanocomposite and nanostructured coatings: Recent advancements. *ACS Symposium Series*, 1008:2–21, 2009.

[24] Veronika Jašková, Libuše Hochmannová, and Jarmila Vytřasová. TiO2 and ZnO nanoparticles in photocatalytic and hygienic coatings. *International Journal of Photoenergy*, 2013, 2013.

[25] Ricardo Solano, David Patiñ O-Ruiz, and Adriana Herrera. Emerging Polymer Based Nanocomposites-Research Article.

[26] Hua Zou, Shishan Wu, and Jian Shen. Polymer/Silica Nanocomposites: Preparation, Characterization, Properties, and Applications. *Chemical Reviews*, 108(9):3893–3957, sep 2008.

[27] M. Abu Tariq, M. Faisal, M. Saquib, and M. Muneer. Heterogeneous photocatalytic degradation of an anthraquinone and a triphenylmethane dye derivative in aqueous suspensions of semiconductor. *Dyes and Pigments*, 76(2):358–365, 2008.

[28] M. A. Rauf, S. B. Bukallah, Amena Hamadi, Azwa Sulaiman, and Fatima Hammadi. The effect of operational parameters on the photoinduced decoloration of dyes using a hybrid catalyst V2O5/TiO2. *Chemical Engineering Journal*, 129(1-3):167–172, 2007.

[29] Niyaz Mohammad Mahmoodi, Mokhtar Arami, Nargess Yousefi Limaee, and Nooshin Salman Tabrizi. Kinetics of heterogeneous photocatalytic degradation of reactive dyes in an immobilized TiO2 photocatalytic reactor. *Journal of Colloid and Interface Science*, 295(1):159–164, 2006.

[30] Vignesh Kumaravel, Muhammad Danyal Imam, Ahmed Badreldin, Rama Krishna Chava, Jeong Yeon Do, Misook Kang, and Ahmed Abdel-Wahab. Photocatalytic hydrogen production: Role of sacrificial reagents on the activity of oxide, carbon, and sulfide catalysts. *Catalysts*, 9(3), 2019.

[31] M Vittoriadiamanti and M P Pedeferri. Concrete, mortar and plaster using titanium dioxide nanoparticles: Applications in pollution control, self-cleaning and photo sterilization. *Nanotechnology in Eco-Efficient Construction: Materials, Processes and Applications*, pages 299–326, 2013.

[32] Adrien Gandolfo, Louis Rouyer, Henri Wortham, and Sasho Gligorovski. The influence of wall temperature on NO2 removal and HONO levels released by indoor photocatalytic paints. *Applied Catalysis B: Environmental*, 209:429–436, 2017.

[33] V. Bartolomei, E. Gomez Alvarez, J. Wittmer, S. Tlili, R. Strekowski, B. Temime-Roussel, E. Quivet, H. Wortham, C. Zetzsch, J. Kleffmann, and S. Gligorovski. Combustion Processes as a Source of High Levels of Indoor Hydroxyl Radicals through the Photolysis of Nitrous Acid. *Environmental Science and Technology*, 49(11):6599–6607, jun 2015.

[34] Alberto Notario, Iván Bravo, José Antonio Adame, Yolanda Díaz-de Mera, Alfonso Aranda, Ana Rodríguez, and Diana Rodríguez. Analysis of NO, NO2, NOx, O3 and oxidant (OX = O3 + NO2) levels measured in a metropolitan area in the southwest of Iberian Peninsula. *Atmospheric Research*, 104-105:217–226, 2012.

[35] Xiaomin Xie, Chenrui Hao, Yue Huang, and Zhen Huang. Influence of TiO2-based photocatalytic coating road on traffic-related NOx pollutants in urban street canyon by CFD modeling. *Science of The Total Environment*, 724:138059, 2020.

[36] Fei Xu, Tao Wang, Hong Yu Chen, James Bohling, Alvin M Maurice, Limin Wu, and Shuxue Zhou. Preparation of photocatalytic TiO2-based self-cleaning coatings for painted surface without interlayer. *Progress in Organic Coatings*, 113(May):15–24, 2017.

[37] F Petronella, A Truppi, C Ingrosso, T Placido, M Striccoli, M L Curri, A Agostiano, and R Comparelli. Nanocomposite materials for photocatalytic degradation of pollutants. *Catalysis Today*, 281:85–100, 2017.

[38] E Vazirinasab, R Jafari, and G Momen. Application of superhydrophobic coatings as a corrosion barrier: A review. *Surface and Coatings Technology*, 341:40–56, 2018.

[39] AKIRA FUJISHIMA and KENICHI HONDA. Electrochemical Photolysis of Water at a Semiconductor Electrode. *Nature 1972 238:5358*, 238(5358):37–38, 1972.

[40] Mark S. Wrighton, Arthur B. Ellis, Peter T. Wolczanski, David L. Morse, Harmon B. Abrahamson, and David S. Ginley. Strontium titanate photoelectrodes. Efficient photoassisted electrolysis of water at zero applied potential. *Journal of the American Chemical Society*, 98(10):2774–2779, may 2002.

[41] Michael R. Hoffmann, Scot T. Martin, Wonyong Choi, and Detlef W. Bahnemann. Environmental Applications of Semiconductor Photocatalysis. *Chemical Reviews*, 95(1):69–96, 2002.

[42] Akira Fujishima, Tata N Rao, and Donald A Tryk. Titanium dioxide photocatalysis. *Journal of Photochemistry and Photobiology C: Photochemistry Reviews*, 1(1):1–21, 2000.

[43] Priyanka Gupta and Vandana Rathore. Study of TiO2material: A photocatalyst for contrary pollutants. *Materials Today: Proceedings*, 42(xxxx):1345–1352, 2020.

[44] Fatemeh Hamidi and Farhad Aslani. Tio2-based photocatalytic cementitious composites: Materials, properties, influential parameters, and assessment techniques. *Nanomaterials*, 9(10), 2019.

[45] Reza Katal, Saeid Masudy-Panah, Mohammad Tanhaei, Mohammad Hossein Davood Abadi Farahani, and Hu Jiangyong. A review on the synthesis of the various types of anatase TiO2 facets and their applications for photocatalysis. *Chemical Engineering Journal*, 384(August 2019):123384, 2020.

[46] M Khalid Hossain, A A Mortuza, S K Sen, M K Basher, M W Ashraf, S Tayyaba, M N H Mia, and M Jalal Uddin. A comparative study on the influence of pure anatase and Degussa-P25 TiO2 nano-materials on the structural and optical properties of dye sensitized solar cell (DSSC) photoanode. *Optik*, 171(May):507–516, 2018.

[47] Xiongzhen Jiang, Maykel Manawan, Ting Feng, Ruifeng Qian, Ting Zhao, Guanda Zhou, Fantai Kong, Qing Wang, Songyuan Dai, and Jia Hong Pan. Anatase and rutile in evonik aeroxide P25: Heterojunctioned or individual nanoparticles? *Catalysis Today*, 300(May 2017):12–17, 2018.

[48] Huanli Wang, Lisha Zhang, Zhigang Chen, Junqing Hu, Shijie Li, Zhaohui Wang, Jianshe Liu, and Xinchen Wang. Semiconductor heterojunction photocatalysts: design, construction, and photocat-alytic performances. *Chemical Society Reviews*, 43(15):5234–5244, 2014.

[49] Seiji Kakuta and Toshiyuki Abe. Photocatalytic activity of Cu2O nanoparticles prepared through novel synthesis method of precursor reduction in the presence of thiosulfate. *Solid State Sciences*, 11(8):1465–1469, 2009.

[50] Chin Boon Ong, Law Yong Ng, and Abdul Wahab Mohammad. A review of ZnO nanoparticles as solar photocatalysts: Synthesis, mechanisms and applications. *Renewable and Sustainable Energy Reviews*, 81(July 2016):536–551, 2018.

[51] Abdinoor A. Jelle, Mohamad Hmadeh, Paul G. O'Brien, Doug D. Perovic, and Geoffrey A. Ozin. Photocatalytic Properties of All Four Polymorphs of Nanostructured Iron Oxyhydroxides. *Chem-NanoMat*, 2(11):1047–1054, nov 2016.

[52] C N C Hitam and A A Jalil. A review on exploration of Fe2O3 photocatalyst towards degra-dation of dyes and organic contaminants. *Journal of Environmental Management*, 258(October 2019):110050, 2020.

[53] Miguel Pelaez, Nicholas T Nolan, Suresh C Pillai, Michael K Seery, Polycarpos Falaras, Athanas-sios G Kontos, Patrick S M Dunlop, Jeremy W J Hamilton, J Anthony Byrne, Kevin O'Shea, Moham-mad H Entezari, and Dionysios D Dionysiou. A review on the visible light active titanium dioxide photocatalysts for environmental applications. *Applied Catalysis B: Environmental*, 125:331–349, 2012.

[54] Biju Mani Rajbongshi. Photocatalyst: mechanism, challenges, and strategy for organic contaminant degradation. *Handbook of Smart Photocatalytic Materials*, pages 127–149, 1 2020.

[55] C Águia, J Ângelo, Luis M Madeira, and A Mendes. Photo-oxidation of NO using an exterior paint - Screening of various commercial titania in powder pressed and paint films. *Journal of Environmental Management*, 92(7):1724–1732, 2011.

[56] Dominique Scalarone, Massimo Lazzari, and Oscar Chiantore. Acrylic protective coatings modi-fied with titanium dioxide nanoparticles: Comparative study of stability under irradiation. *Polymer Degradation and Stability*, 97(11):2136–2142, 2012.

[57] Tina Marolt, Andrijana Sever Škapin, Janez Bernard, Petra Živec, and Miran Gaberšček. Pho-tocatalytic activity of anatase-containing facade coatings. *Surface and Coatings Technology*, 206(6):1355–1361, 2011.

[58] Hedwig M. Braakhuis, Ilse Gosens, Minne B. Heringa, Agnes G. Oomen, Rob J. Vandebriel, Monique Groenewold, and Flemming R. Cassee. Mechanism of Action of TiO2: Recommenda-tions to Reduce Uncertainties Related to Carcinogenic Potential. *Annual Review of Pharmacology and Toxicology*, 61:203–223, 2021.

[59] X-ray powder diffraction (xrd).

[60] Le Qiu, Douglas K. Pleskow, Ram Chuttani, Lei Zhang, Vladimir Turzhitsky, Eric U. Yee, Mandeep Sawhney, Tyler M. Berzin, Fen Wang, Umar Khan, Edward Vitkin, Jeffrey D. Goldsmith, Irving Itzkan, and Lev T. Perelman. In vivo optical detection of dysplasia in barrett's esophagus with endoscopic light scattering spectroscopy. *Barrett's Esophagus: Emerging Evidence for Improved Clinical Practice*, pages 91–104, 1 2016.

[61] Sergej Bock, Christian Kijatkin, Dirk Berben, and Mirco Imlau. applied sciences Absorption and Remission Characterization of Pure , Dielectric (Nano-) Powders Using Diffuse Reflectance Spectroscopy : An End-To-End Instruction. 2019.

[62] Patrycja Makuła and Wojciech Pacia Michałand Macyk. How To Correctly Determine the Band Gap Energy of Modified Semiconductor Photocatalysts Based on UV-Vis Spectra. *Journal of Physical Chemistry Letters*, 9(23):6814–6817, 2018.

[63] R Alcaraz de la Osa, I Iparragirre, D Ortiz, and J M Saiz. The extended Kubelka–Munk theory and its application to spectroscopy. *ChemTexts*, 6(1), 2020.

[64] Mastersizer 3000 — world's leading particle size analyzer — malvern panalytical.

[65] João Figueiredo and Fátima Ramôa Ribeiro. *Catálise Heterogénea, 2nd ed.* Fundação Calouste Gulbenkian, Lisboa, 2007.

[66] Foad Kazemi, Zahra Mohamadnia, Babak Kaboudin, and Zeinab Karimi. Photodegradation of methylene blue with a titanium dioxide/polyacrylamide photocatalyst under sunlight. *Journal of Applied Polymer Science*, 133(19):1–9, 2016.

[67] M. A. Rauf, S. B. Bukallah, Amena Hamadi, Azwa Sulaiman, and Fatima Hammadi. The effect of operational parameters on the photoinduced decoloration of dyes using a hybrid catalyst V2O5/TiO2. *Chemical Engineering Journal*, 129(1-3):167–172, 2007.

[68] M A Rauf and S Salman Ashraf. Fundamental principles and application of heterogeneous photocatalytic degradation of dyes in solution. *Chemical Engineering Journal*, 151(1-3):10–18, 2009.

[69] M. A. Rauf, S. B. Bukallah, Amena Hamadi, Azwa Sulaiman, and Fatima Hammadi. The effect of operational parameters on the photoinduced decoloration of dyes using a hybrid catalyst V2O5/TiO2. *Chemical Engineering Journal*, 129(1-3):167–172, 2007.

[70] Johan P.R. de Villiers and Peter R. Buseck. Mineralogy and instrumentation. *Encyclopedia of Physical Science and Technology*, pages 1–27, 1 2003.

[71] E K Tetteh, S Rathilal, and D B Naidoo. Photocatalytic degradation of oily waste and phenol from a local South Africa oil refinery wastewater using response methodology. *Scientific Reports*, 10(1), 2020.

[72] Jatinder Kumar Ratan, Anil Saini, and Priyanshu Verma. Microsized-titanium dioxide based self-cleaning cement: incorporation of calcined dolomite for enhancement of photocatalytic activity. *MRE*, 5:115509, 11 2018.

[73] Yeob Lee, Sangjun Kim, Honghan Fei, Jeung Ku Kang, and Seth M. Cohen. Photocatalytic CO2 reduction using visible light by metal-monocatecholato species in a metal-organic framework. *Chemical Communications*, 51(92):16549–16552, 2015.

[74] Kezhen Qi, Bei Cheng, Jiaguo Yu, and Wingkei Ho. Review on the improvement of the photocatalytic and antibacterial activities of ZnO. *Journal of Alloys and Compounds*, 727:792–820, 2017.

[75] Riza Ariyani Nur Khasanah, Hui-Ching Lin, Hsiang-Yun Ho, Yen-Ping Peng, Tsong-Shin Lim, Hsi-Lien Hsiao, Chang-Ren Wang, Min-Chieh Chuang, and Forest Shih-Sen Chien. Studies on the substrate-dependent photocatalytic properties of Cu2O heterojunctions. *RSC Advances*, 11(9):4935–4941, 2021.

[76] Rishat Ilmetov. Photocatalytic activity of hematite nanoparticles prepared by sol-gel method. *Materials Today: Proceedings*, 6:11–14, 2019.

[77] A Abdolhoseinzadeh and S Sheibani. Enhanced photocatalytic performance of Cu2O nano-photocatalyst powder modified by ball milling and ZnO. *Advanced Powder Technology*, 31(1):40–50, 2020.

[78] Taeyoung Yang, Seong-jin Park, Taek Gon Kim, Dong Su Shin, Kyung-do Suh, and Jinsub Park. Ultraviolet photodetector using pn junction formed by transferrable hollow n-TiO_2 nano-spheres monolayer. *Optics Express*, 25(25):30843, 2017.

[79] U. Nwankwo, R. Bucher, A. B.C. Ekwealor, S. Khamlich, Malik Maaza, and Fabian I. Ezema. Synthesis and characterizations of rutile-TiO2 nanoparticles derived from chitin for potential photocatalytic applications. *Vacuum*, 161(October 2018):49–54, 2019.

[80] Marcela Chaki Borrás, Ronald Sluyter, Philip J Barker, Konstantin Konstantinov, and Shahnaz Bakand. Y2O3 decorated TiO2 nanoparticles: Enhanced UV attenuation and suppressed photocatalytic activity with promise for cosmetic and sunscreen applications. *Journal of Photochemistry and Photobiology B: Biology*, 207:111883, 2020.

[81] Guanglong Liu, Shuijiao Liao, Duanwei Zhu, Linghua Liu, Dongsheng Cheng, and Huaidong Zhou. Photodegradation of aniline by goethite doped with boron under ultraviolet and visible light irradiation. *Materials Research Bulletin*, 46(8):1290–1295, 2011.

[82] Pratishtha Kushwaha and Pratima Chauhan. Synthesis of spherical and Rod-Like EDTA assisted α-Fe2O3 nanoparticles via Co-precipitation method. *Materials Today: Proceedings*, (xxxx), 2021.
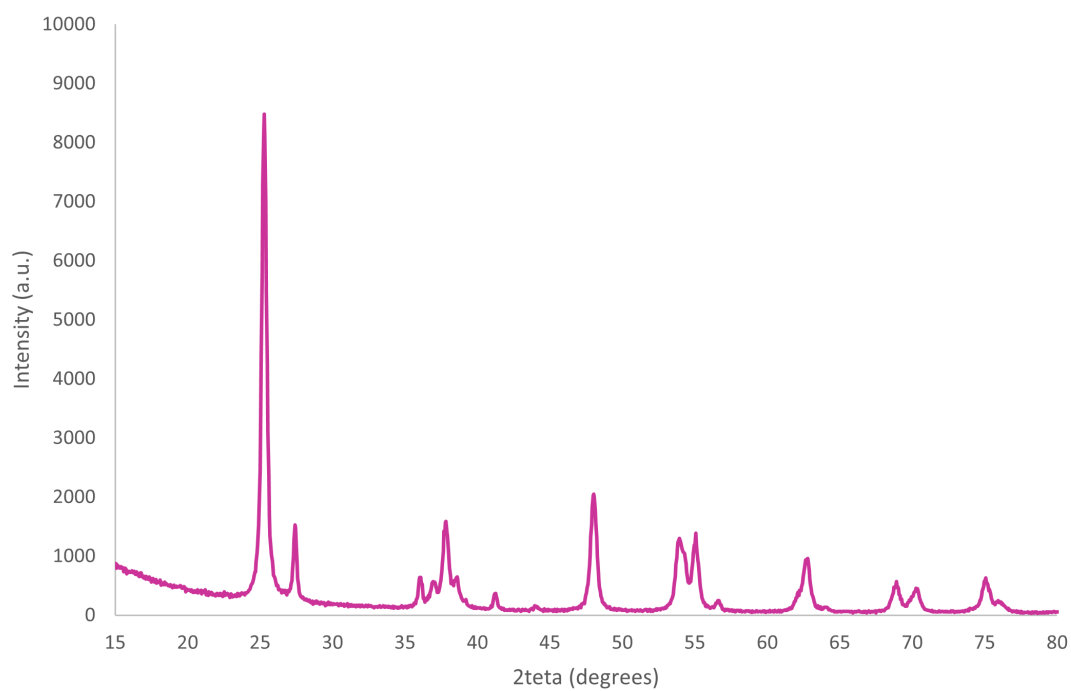
Appendix A
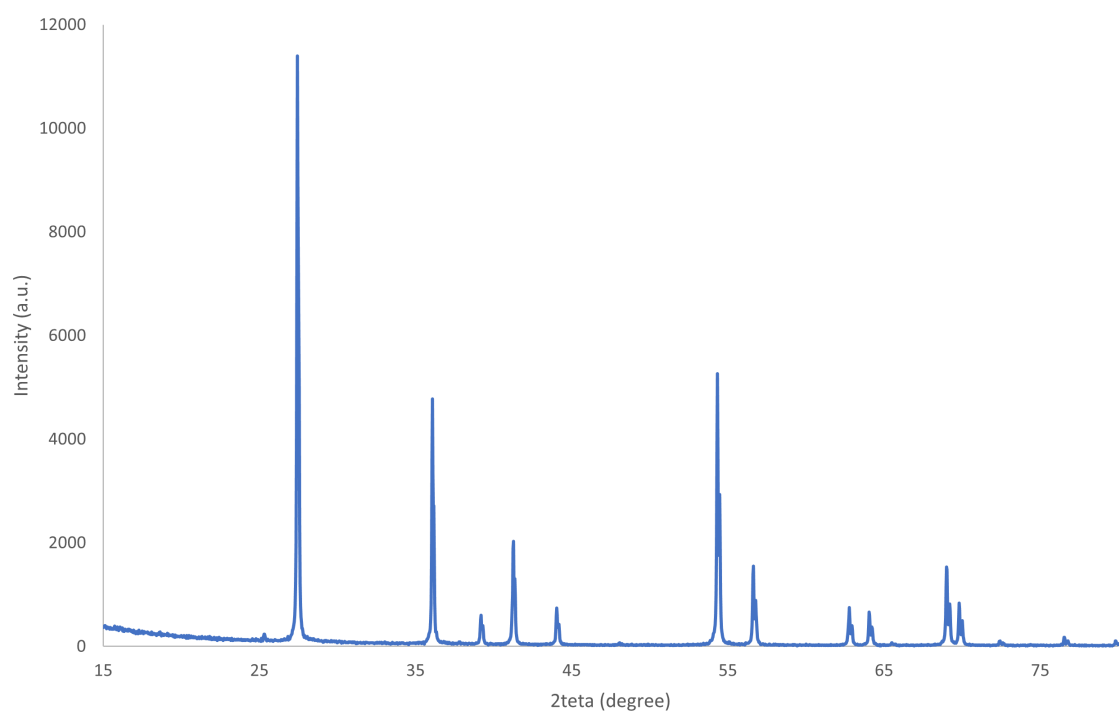
XRD Patterns

Figure A.1: TiO$_2$ P25 XRD pattern.
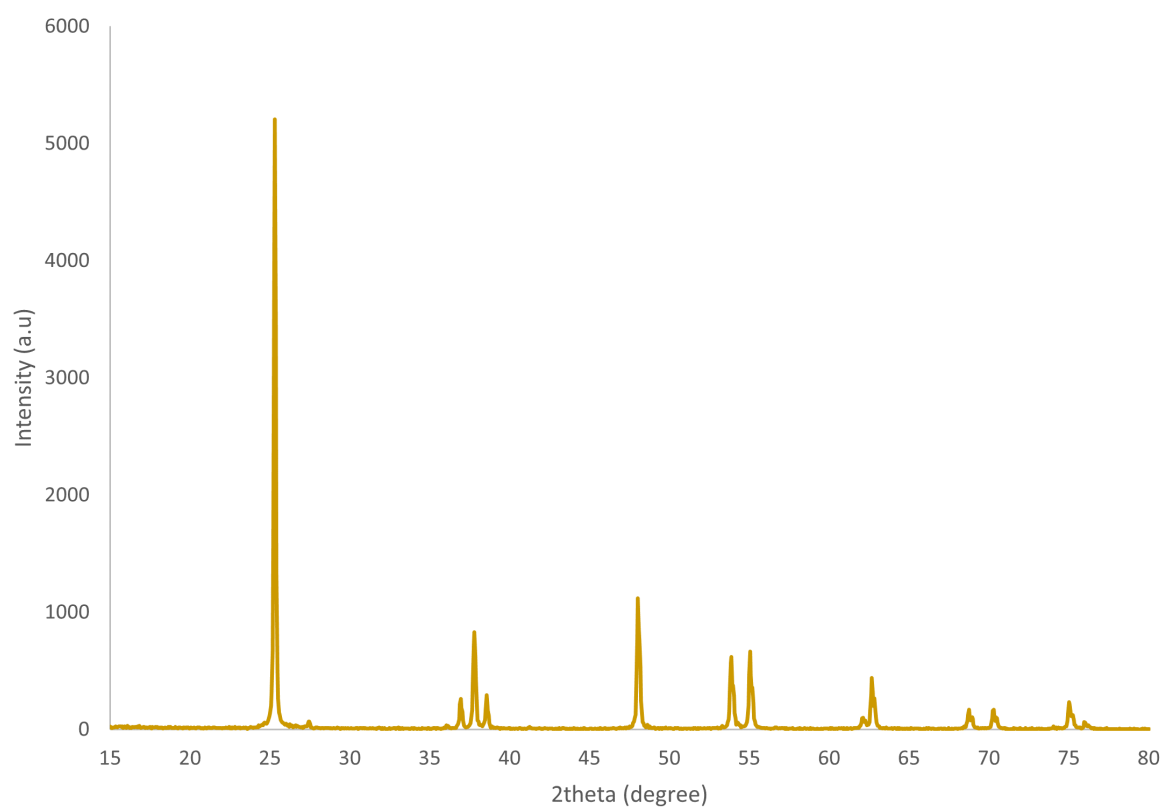
Figure A.2: TiO$_2$ Rutile XRD pattern.

Figure A.3: TiO$_2$ Anatase XRD pattern.
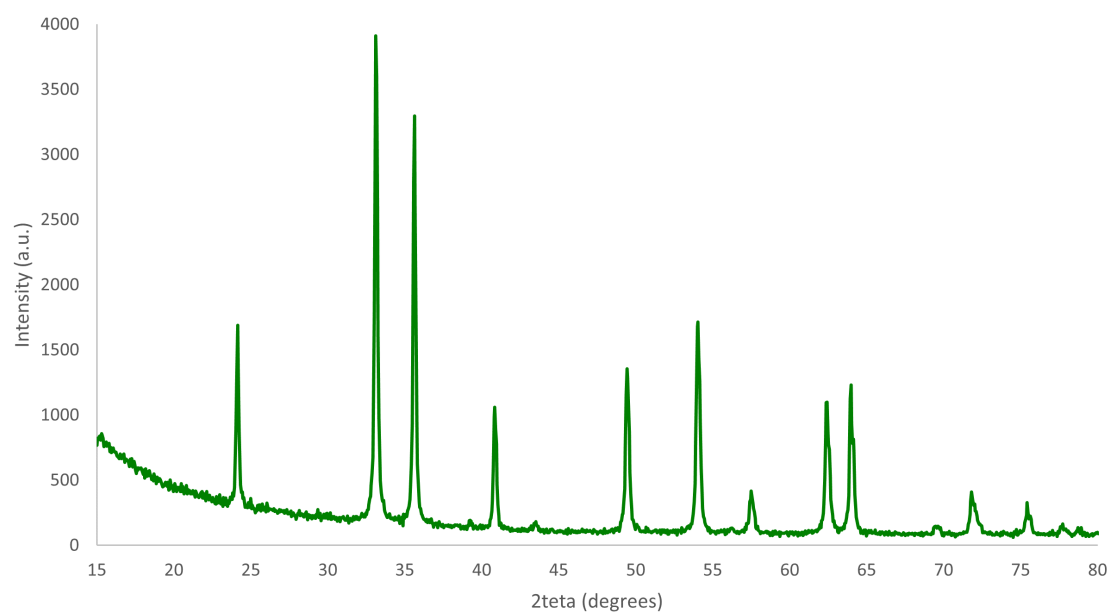
Figure A.4: Fe_2O_3 spherical XRD pattern.
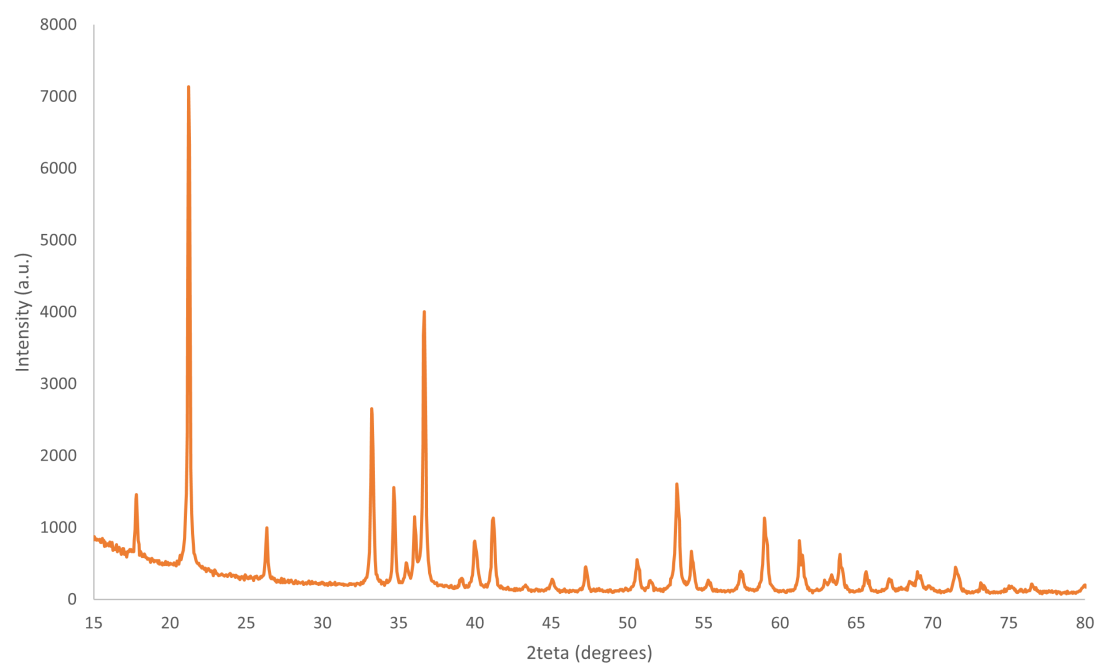

Figure A.5: FeOOH XRD pattern.
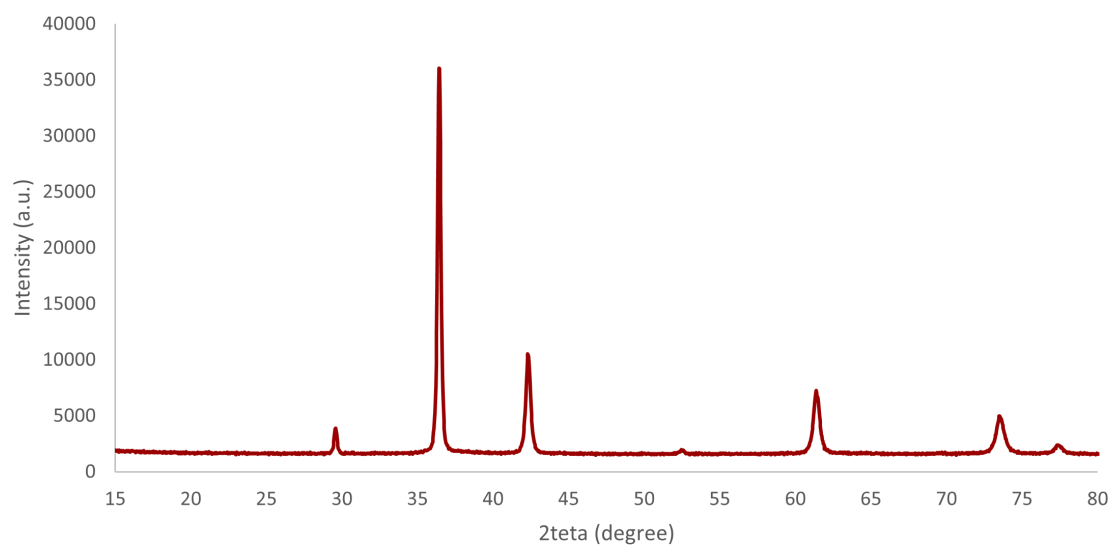
Figure A.6: Cu$_2$O XRD pattern.
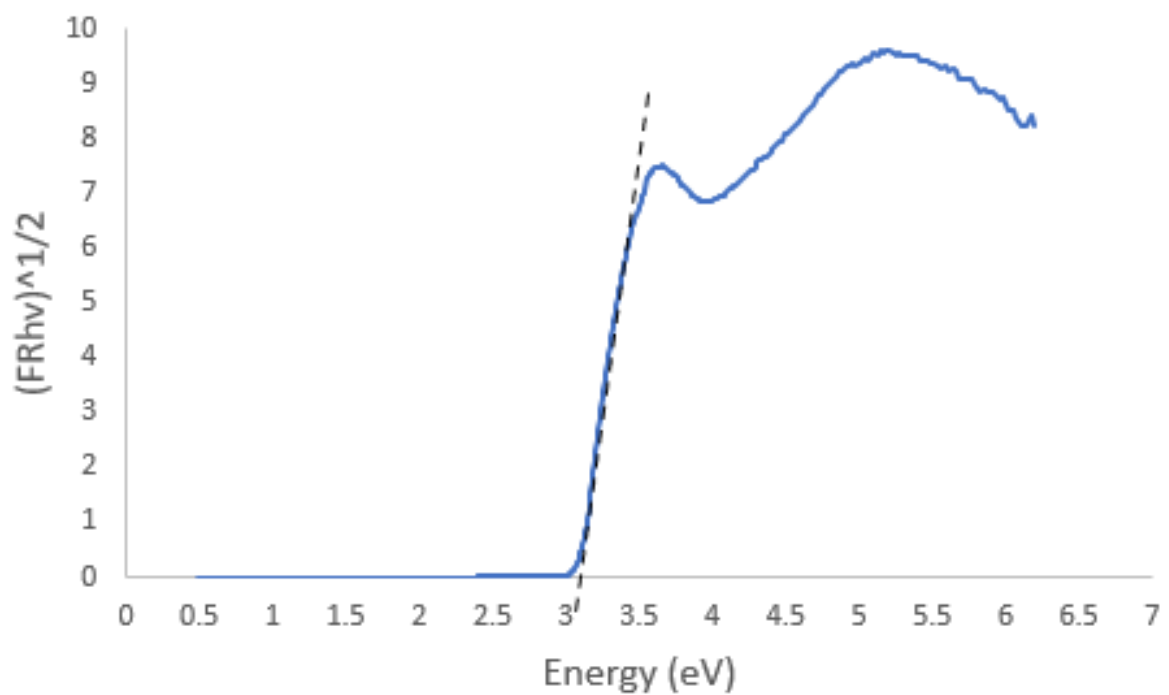
Appendix B

Indirect Tauc Plots
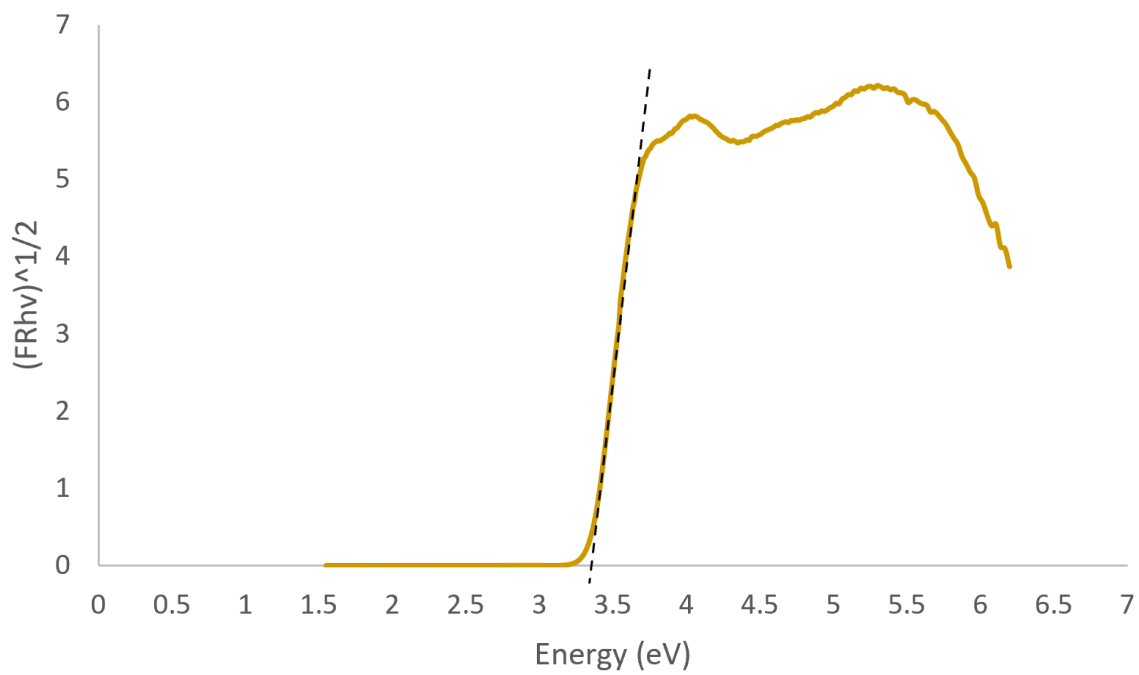

Figure B.1: TiO$_2$ rutile indirect transition.
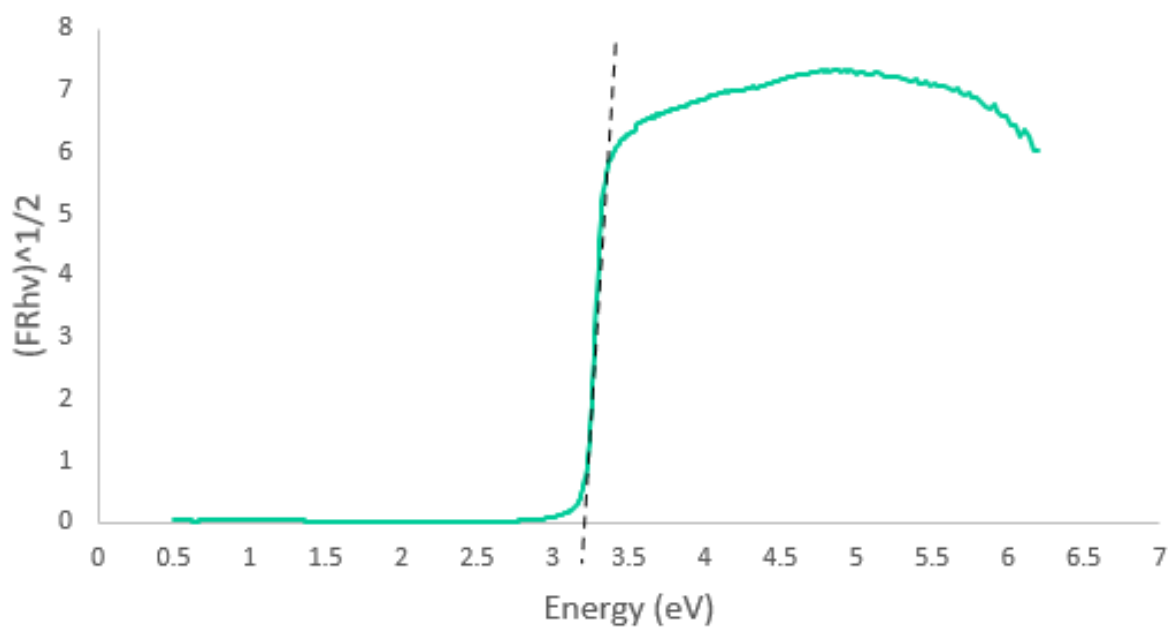
Figure B.2: TiO$_2$ anatase indirect transition.
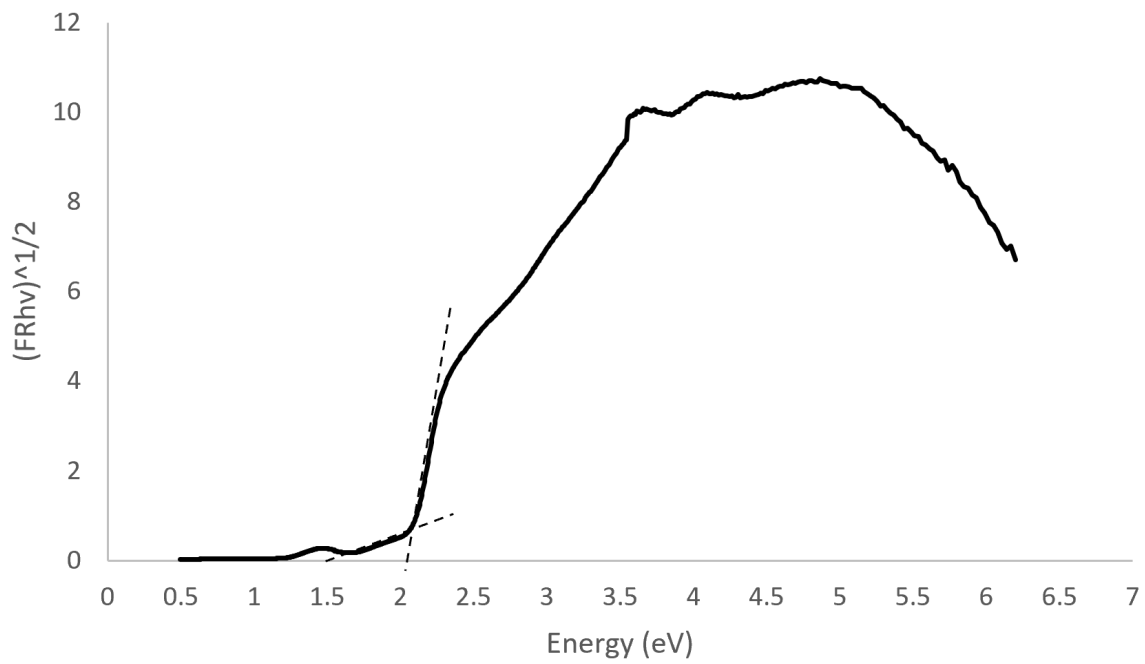

Figure B.3: ZnO indirect transition.

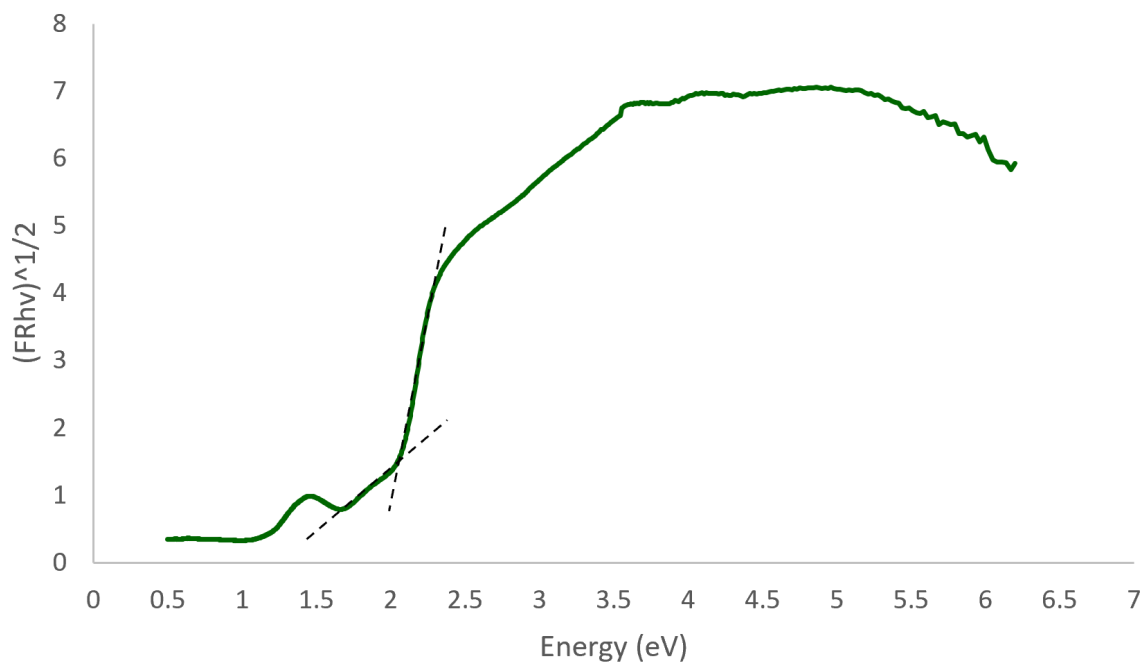Figure B.4: Fe_2O_3 lamellar indirect transition.
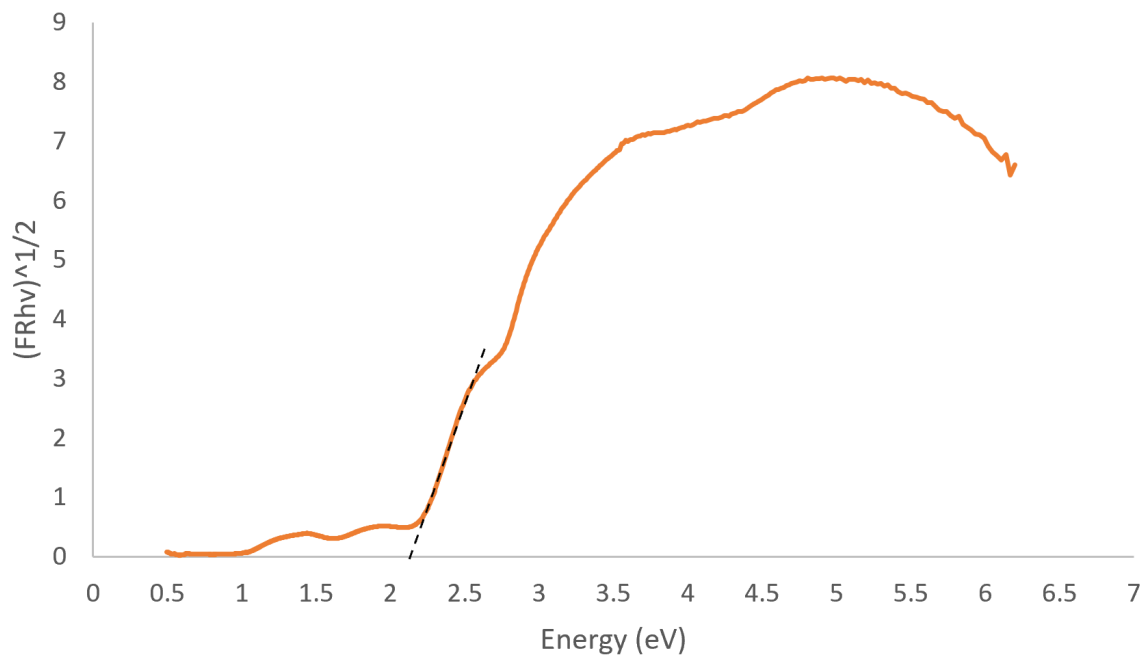

Figure B.5: Fe_2O_3 spherical indirect transition.
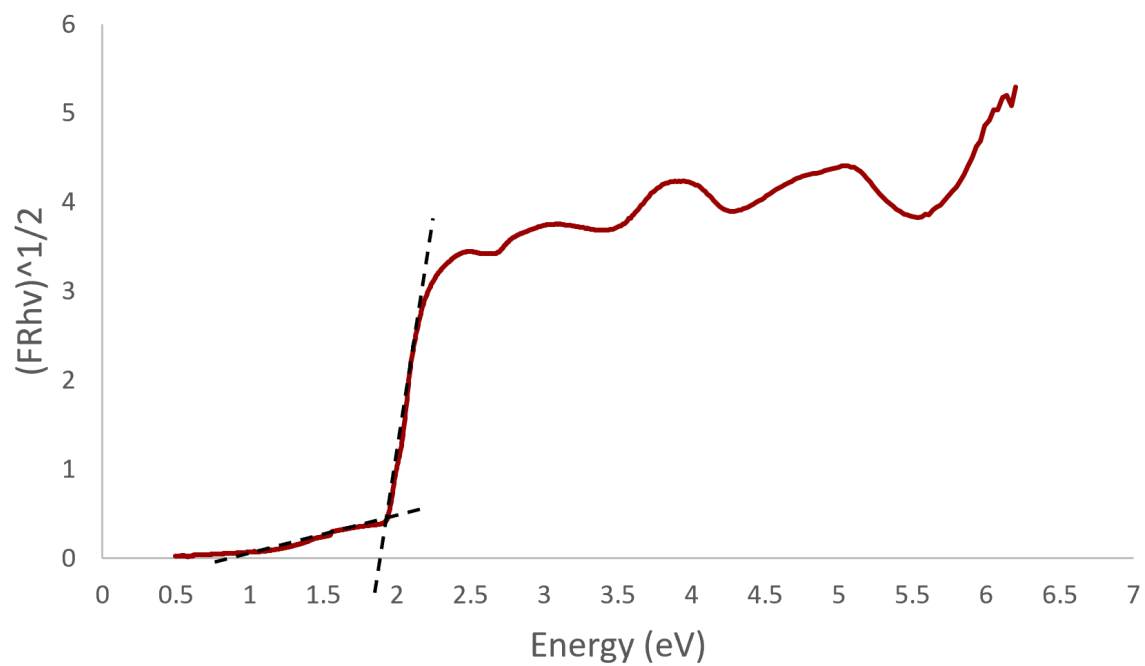
57

Figure B.6: FeOOH indirect transition.

Figure B.7: Cu$_2$O indirect transition.

Appendix C

Excel Data Analysis

Regression Statistics	
Multiple R	0.995793
R Square	0.991604
Adjusted R Square	0.991462
Standard Error	0.062894
Observations	61

ANOVA

	df	SS	MS	F	Significance F
Regression	1	27.5646	27.565	6968.465	5.97E-63
Residual	59	0.23338	0.0040		
Total	60	27.7980			

	Coefficients	Standard Error	t Stat	P-value	Lower 95%	Upper 95%	Lower 95.0%	Upper 95.0%
Intercept	-21.4546	0.2766	77.582	4.33E-61	-22.0079	-20.901	-22.008	-20.901
X Variable 1	11.24888	0.1348	83.477	5.97E-63	10.97924	11.519	10.979	11.519
Eg	**1.907263**							

Figure C.1: Example of how to calculate the BG resorting to *Data Analysis* on Excel.